

Structural Diversity of Lanthanide 3-Nitrotrispyrazolylborates: Tunable Nuclearity and Intra-Ligand Charge Transfer Sensitization of Visible and NIR Ln^{3+} Emission

Christopher H. Hossack,[†] Raymond J. Butcher,[‡] Christopher L. Cahill,[†] Claire Besson*,[†]

[†]Department of Chemistry, The George Washington University, 800 22nd Street, NW, Washington, D.C. 20052, United States

[‡]Department of Chemistry, Howard University, 525 College St. N.W., Washington, DC 20059, United States

ABSTRACT: Reported are the synthesis, crystal structures and photophysical properties of twenty-eight, novel lanthanide compounds across five structural types, $[\text{Ln}(3\text{-NO}_2\text{Tp})_2(\text{NO}_3)]$ (**1-Ln**, Ln = La – Tm, except Pm), $[\text{Bu}_4\text{N}][\text{Ln}(3\text{-NO}_2\text{Tp})(\text{NO}_3)_3]$ (**2-Ln**, Ln = Yb, Lu), $[\text{Eu}(3\text{-NO}_2\text{Tp})_2\text{Cl}(\text{H}_2\text{O})] \cdot 2\text{PrOH}$ (**3-Eu**), $[\{\text{Ln}(3\text{-NO}_2\text{Tp})_2\}_2(\mu_2\text{-CO}_3)]$ (**4-Ln**, Ln = La – Gd, except Pm) and $[\{\text{Ln}(3\text{-NO}_2\text{Tp})\}_4(\mu_2\text{-OMe})_6(\mu_4\text{-O})]$ (**5-Ln**, Ln = Pr – Tb, except Pm) with the 3-nitrotrispyrazolylborate ($3\text{-NO}_2\text{Tp}^-$) ligand. Reaction of methanol or isopropanol solutions of LnX_3 (X = Cl, NO_3) with the tetrabutyl ammonium salt of the flexidentate $3\text{-NO}_2\text{Tp}^-$, $([\text{Bu}_4\text{N}][3\text{-NO}_2\text{Tp}])$ yields $\text{Ln}(3\text{-NO}_2\text{Tp})_x$ complexes of various nuclearities as either monomers (**1-Ln**, **2-Ln**, **3-Eu**), dimers (**4-Ln**) or tetramers (**5-Ln**) owing to the efficient conversion of atmospheric CO_2 to CO_3^{2-} (dimers) or ligand controlled solvolysis of lanthanide ions (tetramers). $3\text{-NO}_2\text{Tp}^-$ is an efficient sensitizer for both the visible and near-IR (NIR) emissions of most of the lanthanide series, except thulium. Optical measurements, supported by density functional theory calculations, indicate that the dual visible and NIR Ln^{3+} emission arises from two intra-ligand charge transfer (ILCT) transitions of $3\text{-NO}_2\text{Tp}^-$. This is the first

report of lanthanide complexes with a nitro-functionalized pyrazolylborate ligand. The derivatization of the known Tp^- ligand results in new coordination chemistry governed by the increased denticity of $3\text{-NO}_2\text{Tp}^-$, imparting remarkable structural diversity and charge transfer properties to resultant lanthanide complexes.

1. Introduction

There is considerable interest in the discovery of new lanthanide (Ln)-containing materials due to their unique, intrinsic magnetic and photophysical properties and the desire to design functional Ln-materials for specific applications.^{1, 2} This is typically achieved *via* the judicious choice of an organic ligand with desirable properties, to generate hybrid (organic-inorganic) materials, where the ligand can influence which lanthanide property(ies) are expressed. In particular, lanthanide complexes with pyrazolylborate ligands, are of interest to researchers as they display single molecule magnet properties,^{3, 4} sensitized Ln^{3+} emission^{5, 6} as well as C-H activation catalysis.⁷⁻⁹ Lanthanide pyrazolylborate complexes, despite their promising chemical and physical properties, are still relatively underexplored, with only a limited range of pyrazolylborates used.^{10, 11}

Pyrazolylborates are pyrazole-substituted derivatives of the borohydride, BH_4^- ion, discovered by Trofimenko over 50 years ago.¹² Trispyrazolylborate (Tp^-), where three of the four hydrides are replaced by pyrazole rings, is the most well-studied type of pyrazolylborate owing to its strong chelating ability. A recent development in the chemistry of pyrazolylborates by Besson and coworkers, made it possible to selectively functionalize the pyrazole backbone of Tp^- ligands with strongly electron-donating or withdrawing groups (Figure 1).^{13, 14} This is promising as most lanthanide-trispyrazolylborate complexes use either the non-functionalized Tp^- or feature simple short-chain alkyl groups (e.g. methyl or isopropyl), that do not

substantially change the electronic properties of Tp^- .¹¹ The introduction of functional groups, like the nitro-group (NO_2^-), that can drastically modify the electronic structure of Tp^- , thus provides the opportunity to design new Tp^- ligands to manipulate the properties of resultant Ln-Tp complexes.

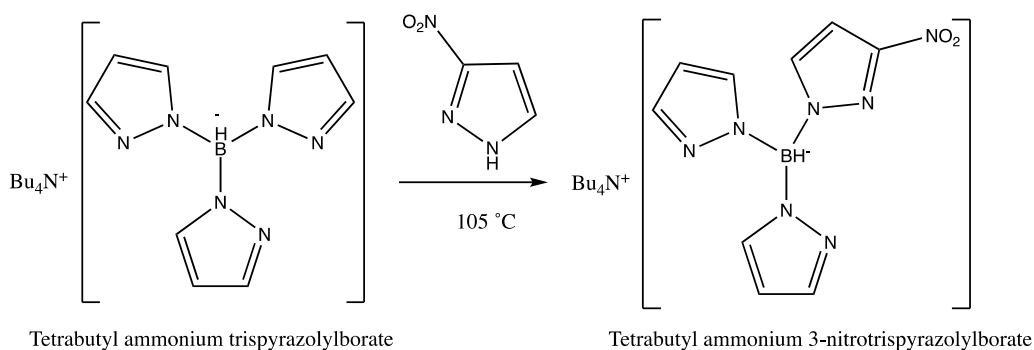


Figure 1: Synthesis of 3-nitrotrispyrazolylborate.

Nitro-functionalized ligands have been reported to introduce structural diversity to lanthanide hybrid materials in the form of nanoclusters,¹⁵ coordination polymers¹⁶ and MOFs¹⁷. Moreover, nitrated ligands are bulkier than their non-functionalized analogues, which may allow them to function as capping ligand for higher nuclearity lanthanide complexes.¹⁸ Beyond structure-directing properties, the introduction of a nitro-group can also impact photophysical properties. De Bettencourt Dias and coworkers were the first to report any sensitized Ln^{3+} emission with a nitrated aromatic ligand, 4-nitro-3-thiophen-3-yl benzoic acid.¹⁹ Since then, there have been several reports of sensitized Ln^{3+} emission with nitrated ligands including other benzoates,²⁰⁻²⁴ salicylates,²³ oxyquinolates,²³ anthranylates,²³ pyridines²⁵ and salicylaldehydes,²⁶ and even enhancement of Eu^{3+} emission with some nitrated salicylate and oxyquinolate over benzoate ligands.²³

Nitro-groups are also known to deactivate aromatic rings, by pulling electron density away from the π system. This results in a decrease in the energy of π^* orbitals in π -acceptor ligands in organometallic complexes,²⁷ as well as the reduction of the lowest lying triplet state,

T_1 energies in lanthanide antenna ligands like benzoates,²²⁻²⁴ salicylates²³ and pyridines²⁵ as a consequence of decreasing the energy of the π^* orbitals. Antenna ligands are organic chromophores coordinated to lanthanide centers that can transfer energy absorbed from $\pi \rightarrow \pi^*$ or $n \rightarrow \pi^*$ transitions, *via* the ligands' T_1 states, to lanthanide ($^{2S+1}L_J$) states following the Förster resonant energy transfer mechanism.²⁸ This process is distance-dependent and may be enhanced with nitrated antenna ligands that may possess more Ln-ligand bonds and have T_1 energy levels that can be tailored for specific Ln^{3+} states.

In some cases, however, the presence of a nitro-group has been used to explain weak, Ln^{3+} emission intensities, or lack thereof,²⁹ owing to: 1) intra-ligand charge transfer (ILCT) transitions between the π^* orbitals and lone pair p-orbitals of the O in the nitro-group and 2) very short lifetime of the $T_1(\pi^*)$ state and 3) rapid non-radiative decay of the $T_1(\pi^*)$ to the ligand ground state, without energy transfer to Ln^{3+} . Moreover, Cirić and Nikolić reported that the nitro-group can reduce the basicity of the coordinating N of pyrazole rings attributed to a lowering of the net electron density associated with the π electrons of the ring.³⁰ With these reports in mind, we anticipate that use of a partially nitrated trispyrazolylborate ligand, 3-nitrotrispyrazolylborate ($3\text{-NO}_2\text{Tp}^-$) (Figure 1), we will be able to leverage both the desirable structure-directing and photophysical properties associated with the nitro-group while minimizing detrimental impacts on Ln^{3+} emission.

We present herein five lanthanide-3-nitrotrispyrazolylborate complexes, $\text{Ln}(3\text{-NO}_2\text{Tp})_x$ ($\text{Ln} = \text{La} - \text{Lu}$, except Pm) of variable nuclearity together with their photophysical properties. Monomeric, dimeric and tetrameric complexes can be selectively and reproducibly synthesized *via* meticulous control of the initial reaction conditions, including the counterion of the lanthanide starting material, the solvent, the availability of atmospheric CO_2 and the size of the Ln^{3+} ion. Single-crystal X-ray diffraction and infrared spectroscopy confirm the coordination of the nitro-group to select lanthanide centers and the variable denticity in the

3-NO₂Tp⁻ ligand. Room temperature diffuse reflectance (solid-state absorption) and luminescence spectra, supported by DFT and TD-DFT calculations indicate interesting Ln³⁺-3-NO₂Tp⁻ and Ln³⁺-to-Ln³⁺ interactions, attributable to the nitro- functionalization of the Tp⁻ ligand.

2. Results and Discussion

2.1. Synthesis of lanthanide 3-nitrotrispyrazolylborate Ln(3-NO₂Tp)_x complexes

The slow evaporation of solutions of lanthanide salts and 3-NO₂Tp⁻ in methanol or isopropanol, with modifications to the Ln³⁺:3-NO₂Tp⁻ ratio dependent on the desired phase, yields a range of structurally diverse lanthanide 3-nitrotrispyrazolylborate Ln(3-NO₂Tp)_x complexes (Figure 2). Three monomers, [Ln(3-NO₂Tp)₂(NO₃)] (**1**-Ln, Ln = La – Tm, except Pm), [Bu₄N][Ln(3-NO₂Tp)(NO₃)₃] (**2**-Ln, Ln = Yb, Lu), [Eu(3-NO₂Tp)₂Cl(H₂O)] (**3**-Eu), a dimer, [{Ln(3-NO₂Tp)₂]₂(μ₂-CO₃)] (**4**-Ln, Ln = La – Gd, except Pm) and a tetramer, [{Ln(3-NO₂Tp)]₄(μ₂-OMe)₆(μ₄-O)] (**5**-Ln, Ln = Pr – Tb, except Pm) comprise the reported Ln(3-NO₂Tp)_x complexes. Given the mild nature of the reaction conditions, it is surprising to find such diversity in the speciation of resultant lanthanide complexes. The impact of synthetic conditions on the nuclearity of Ln(3-NO₂Tp)_x complexes will be discussed in a later section. Full synthetic details are given in the Experimental Section.

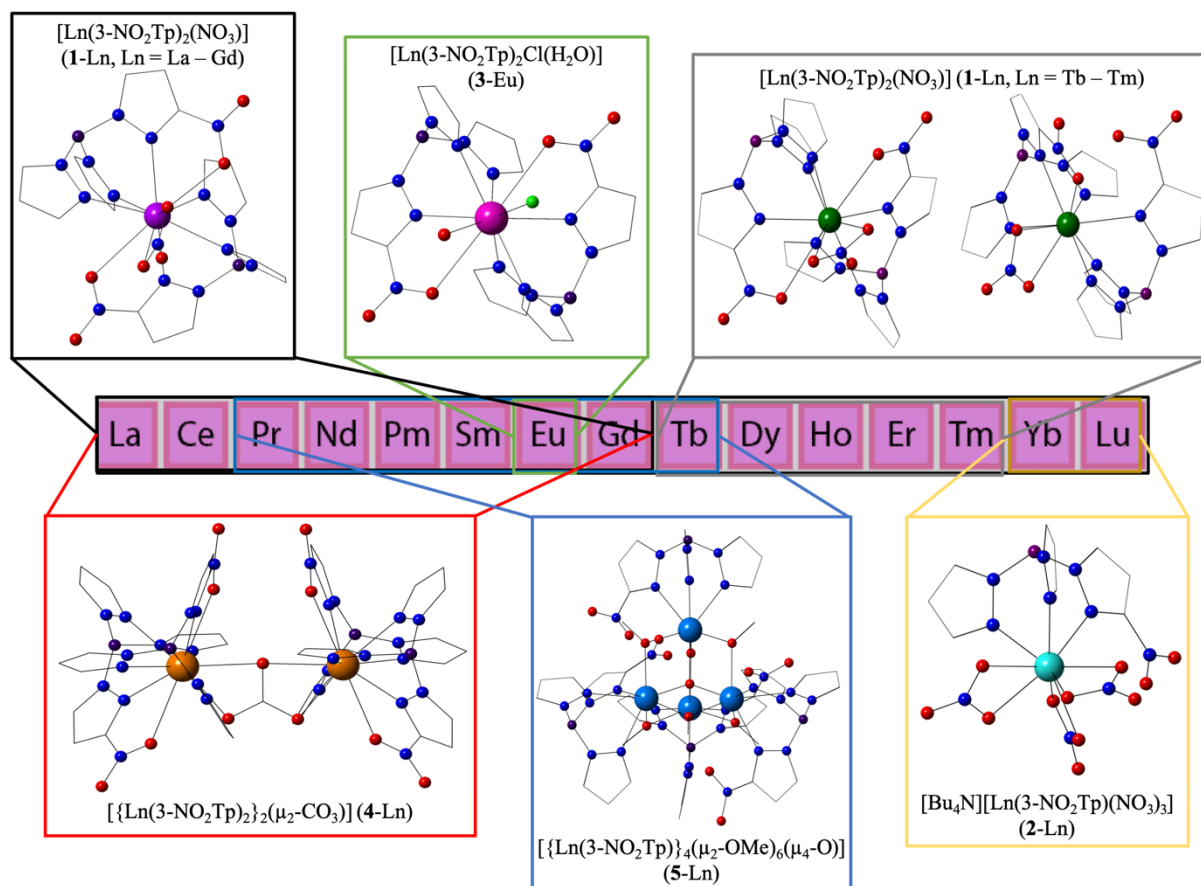


Figure 2: Tunable nuclearity of Ln(3-NO₂Tp)_x structures featuring monomeric (**1-Ln**, **2-Ln**, **3-Eu**), dimeric (**4-Ln**) and tetrameric (**5-Ln**) complexes.

2.2. Structural Descriptions

2.2.1. Mononuclear Complexes

[Ln(3-NO₂Tp)₂(NO₃)] (**1-Ln**, Ln = La – Tm, except Pm)

1-Ln displays polymorphism where **1-La – 1-Gd** and **1-Tb – 1-Tm** constitute two distinct crystalline phases. Based on the crystal structures of **1-Gd** and **1-Ln** (Ln = Dy – Tm), the two phases arose due to the variable coordination modes of the 3-NO₂Tp⁻ ligand, resulting in two coordination isomers of the [Ln(3-NO₂Tp)₂(NO₃)] monomer. The **1-La – 1-Gd** phase display ten coordinate monomers exclusively, whereas ten and nine coordinate monomers can be found in the **1-Tb – 1-Tm** phase. Ten coordinate monomers feature, in addition to a bidentate nitrate, two tetradentate 3-NO₂Tp⁻ ligands where the traditional coordination through the pyrazole nitrogens is completed by the formation of a bond between the nitro-group and the

Ln^{3+} center. Nine coordinate monomers have one tetradentate and one classical tridentate $3\text{-NO}_2\text{Tp}^-$ ligand (Figure 3), in addition to the nitrate ligand.

The first polymorph of **1**-Ln consists of the larger lanthanides from lanthanum to gadolinium, which was confirmed by overlaying their experimental power patterns (**1**-La – **1**-Eu) with the simulated pattern of **1**-Gd (ESI Figure S2). Despite several repeat syntheses and attempts at recrystallization, no suitable crystals for X-ray diffraction of **1**-Ln (Ln = La – Eu) have been isolated, as such, only the crystal structure of **1**-Gd will be discussed in detail. The asymmetric unit of **1**-Gd contains one crystallographically unique monomer (Figure 4(a)) and one fourth of a water molecule. Each monomer consists of two chelating tetradentate $3\text{-NO}_2\text{Tp}^-$ ligands coordinated with Gd–N bond distances ranging from 2.491(3) Å to 2.565(3) Å and Gd–O_{NO2} bond distances that range between 2.893(4) Å and 2.926(2) Å. Further coordination to the Gd^{3+} occurs with a chelating nitrate ligand with Gd–O bond distances from 2.477(2) to 2.494(2) Å. The ten-coordinate Gd^{3+} center adopts a distorted bicapped square anti-prism geometry with approximate D_{4d} site symmetry (Figure 3(b)) and the distance between the two monomers (Gd—Gd) is 8.979(9) Å. The monomers are assembled *via* one unique offset π - π stacking interaction between a pair of nitrated and non-nitrated pyrazole rings only with $C_{gPz}\cdots C_{g3NO2Pz}$ distances of 3.542(1) Å and $\beta = 19.2^\circ$ (Figure 4(b)).

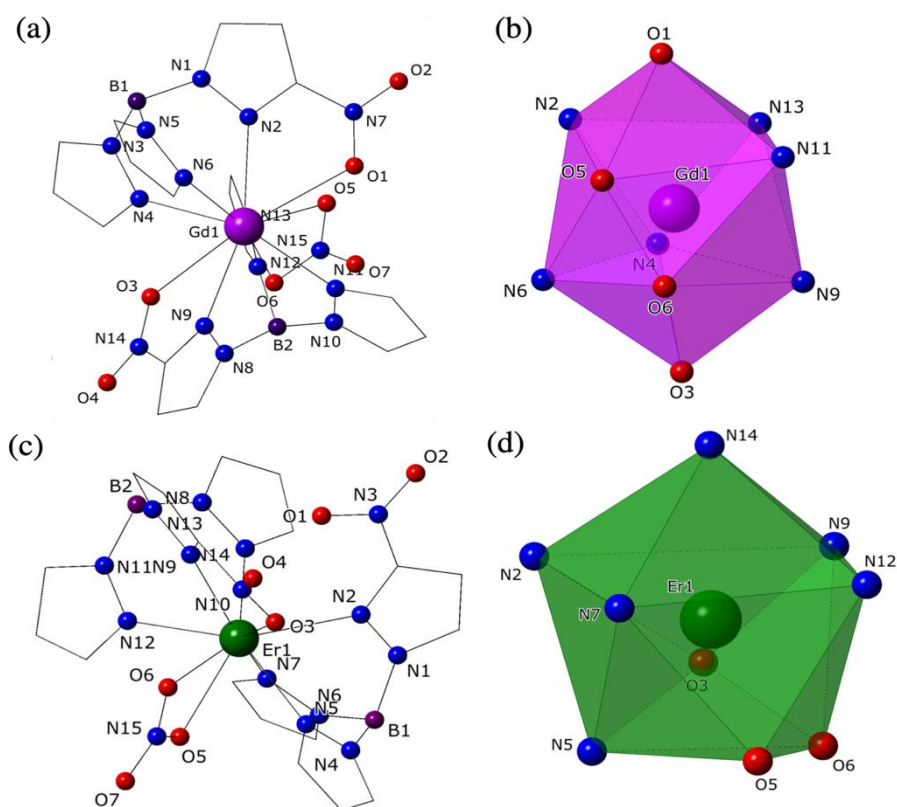


Figure 3: (a) Ten coordinate monomer in **1-Gd** with nitro- groups both coordinated to gadolinium, and on opposite sides of the metal center. (b) Coordination polyhedron of the ten coordinate monomer featuring the ten coordinate, bicapped square antiprism geometry. (c) Nine coordinate monomer from **1-Er**, where only one nitro-group is coordinated to the erbium center and the nitro groups face each other. (d) Coordination polyhedron of the nine coordinate monomer displaying a highly distorted mono-capped square antiprism geometry.

The second polymorph of **1-Ln** is obtained for the smaller lanthanides from terbium to thulium. Four of the five analogues of **1-Ln** ($\text{Ln} = \text{Dy} - \text{Tm}$) are isomorphous, yet crystals of the Tb complex suitable for X-ray diffraction could not be isolated. The PXRD pattern of **1-Tb**, however, was consistent with this polymorph of **1-Ln** (ESI Figure S3). **1-Er** will be discussed in detail as a representative structure for this polymorph. The asymmetric unit in **1-Er** contains two crystallographically unique monomers (Figure 4(c)). The first monomer is ten coordinate, identical to the monomers in **1-Gd**, with two tetradentate 3- NO_2Tp^- ligands and a chelating nitrate coordinated to Er^{3+} , with Er–N distances between 2.46(1) Å and 2.52(1) Å, Er– ONO_2 (O1, O3) distances of 2.78(1) and 3.05(1) Å and Er– ONO_3 (O5, O6) at 2.42(1) Å. The other monomer is nine coordinate with one tetradentate 3- NO_2Tp^- ligand, one tridentate 3- NO_2Tp^- ligand and the chelating nitrate ligand (Figure 4(c)) and is related to the ten

coordinate by de-coordination of the NO₂-group and rotation of the 3-NO₂Tp⁻ ligand by 120° around the Er-B axis. Er–N distances range between 2.39(1) Å and 2.58(1) Å, Er–O_{NO₂} (O8) distance of 2.609(9) Å and Er–O_{NO₃} (O12, O13) at 2.46(1) and 2.38(1)Å respectively. The ten coordinate monomer features the same distorted bicapped square antiprism geometry as in **1**-Gd, whereas the nine coordinate Er³⁺ sites display a highly distorted mono-capped square antiprism geometry (Figure 3(d)). The Er—Er distance between the two monomers is 9.000(3) Å. There are two unique offset π - π stacking interactions throughout the lattice **1**-Er, one between 3-nitropyrazole rings only and the other between pyrazole and 3-nitropyrazole rings, that alternate between ten coordinate and nine coordinate monomers (Figure 4(d)). For the π - π interaction between nitrated rings only, the Cg_{3NO₂Pz}⋯Cg_{3NO₂Pz} distances are 3.4441(15) Å and $\beta = 14.7^\circ$, whereas for the interaction between non-nitrated and nitrated pyrazole rings, the Cg_{Pz}⋯Cg_{3NO₂Pz} distances are 3.5890(15) Å and $\beta = 15.8^\circ$

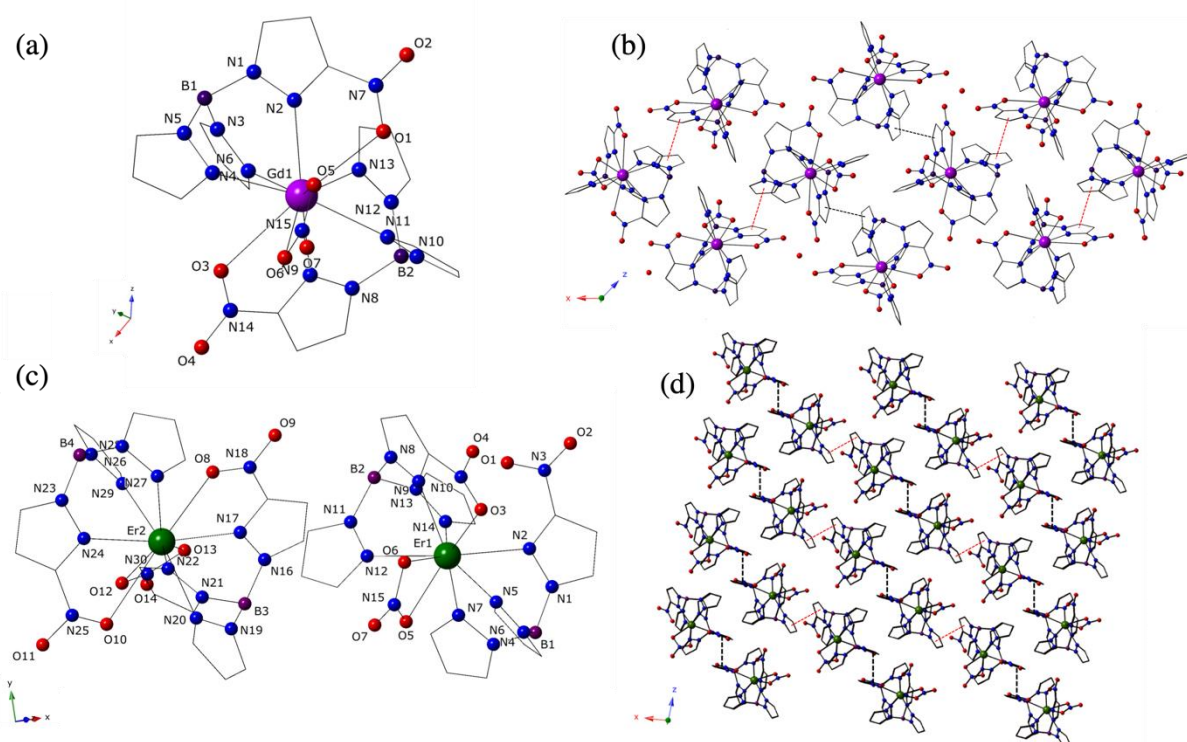


Figure 4: (a) Asymmetric unit of **1**-Gd (solvent methanol omitted for clarity). (b) Packing diagram of **1**-Gd along the c-axis with the two unique offset π - π stacking interactions represented by black and red dashed lines. (c) The asymmetric unit of **1**-Er with one ten coordinate monomer and one nine coordinate monomer. (b) Packing diagram of **1**-Er along c-axis with the two unique offset π - π stacking interaction represented by black and red dashed lines.

[Bu₄N][Ln(3-NO₂Tp)(NO₃)₃] (**2**-Ln, Ln = Yb, Lu)

Complexes of **2**-Ln (Ln = Yb, Lu) are isomorphous and crystallize in the *P2₁/c* space group. The **2**-Yb structure is representative and will be discussed herein. The asymmetric unit of **2**-Yb contains one crystallographically unique Yb³⁺ ion coordinated to one tridentate 3-NO₂Tp⁻ ligand and three chelating nitrate ligands (Figure 5(a)). The resulting anion is charge balanced by a tetrabutylammonium cation and the ion pair make up the asymmetric unit. Each Yb³⁺ ion is nine-coordinate, with Yb–N (N2, N4, N6) distances between 2.401(2) Å and 2.550(2) Å and Yb–O (O3, O4, O6, O7, O9, O10) distances that range from 2.366(2) to 2.461 Å. The YbN₃O₆ polyhedron adopts a distorted mono-capped square antiprism geometry (Figure 5(b)). There are no significant non-covalent interactions between the *tert*-butyl ammonium and [Yb(3-NO₂Tp)(NO₃)₃]⁻ ions or between [Yb(3-NO₂Tp)(NO₃)₃]⁻ anions in the crystal lattice of **2**-Yb (Figure 5(c)). The Yb—Yb distance between ion pairs is 9.303(2) Å.

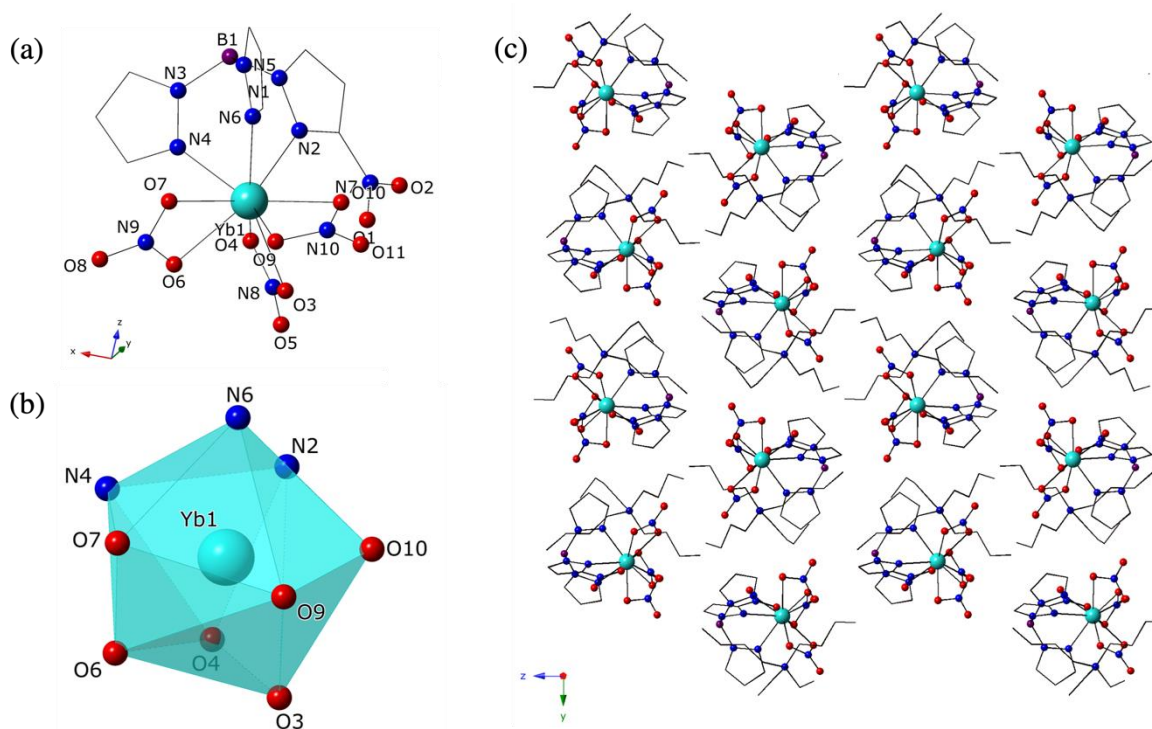


Figure 5: (a) Monomer of **2**-Yb with only one 3-NO₂Tp⁻ coordinated ligand. (b) Coordination polyhedron of the Yb³⁺ ion featuring a highly distorted monocapped square antiprism coordination geometry. (c) Packing diagram of **2**-Yb.

[Eu(3-NO₂Tp)₂Cl(H₂O)]·2ⁱPrOH (**3**-Eu)

3-Eu crystallizes in the $P2_1/c$ space group with one unique Eu³⁺ center coordinated to two tetradentate 3-NO₂Tp⁻ ligands, a chloride and a water ligand, with two isopropanol molecules in the asymmetric unit. This complex is analogous to the ten coordinate monomers of **1**-Ln, substituting the nitrate ligand for chloride and water ligands. Eu–N (N2, N4, N6, N9, N11, N13) distances range from 2.544(3) Å to 2.577(3) Å and Eu1–O_{NO2} (O1, O3) distances were 2.986(3) Å and 2.984 Å respectively. The Eu1–Cl1 bond distance is 2.808(1) Å whereas the Eu1–O5 distance is 2.412(2) Å. The Eu³⁺ center is ten coordinate adopting a distorted, bicapped square antiprism geometry, analogous to the ten coordinate isomer of [Ln(3-NO₂Tp)₂(NO₃)], substituting the nitrate for a chloride and water ligands. There are four unique hydrogen bonding interactions present throughout the lattice between adjacent monomers and isopropanol molecules (Figure 6b)), Cl1(**3**-Eu)—O5(**3**-Eu') at 3.201(10)Å, Cl1—O7(isopropanol) at 2.947(9)Å, O5—O6(isopropanol) at 2.653(8)Å and O6(isopropanol)—O7(isopropanol) at 2.761(9)Å. Hydrogen bonded “dimers” of Eu(3-NO₂Tp)Cl(H₂O), with Eu—Eu distances of 7.467(1) Å, assemble further *via* offset π - π stacking interactions with other dimers between the 3-nitropyrazole rings of the 3-NO₂Tp⁻ ligands (Figure 6(d)) with Cg...Cg distances of 3.345(11) Å and $\beta = 23.5^\circ$ (Figure 6(c)).

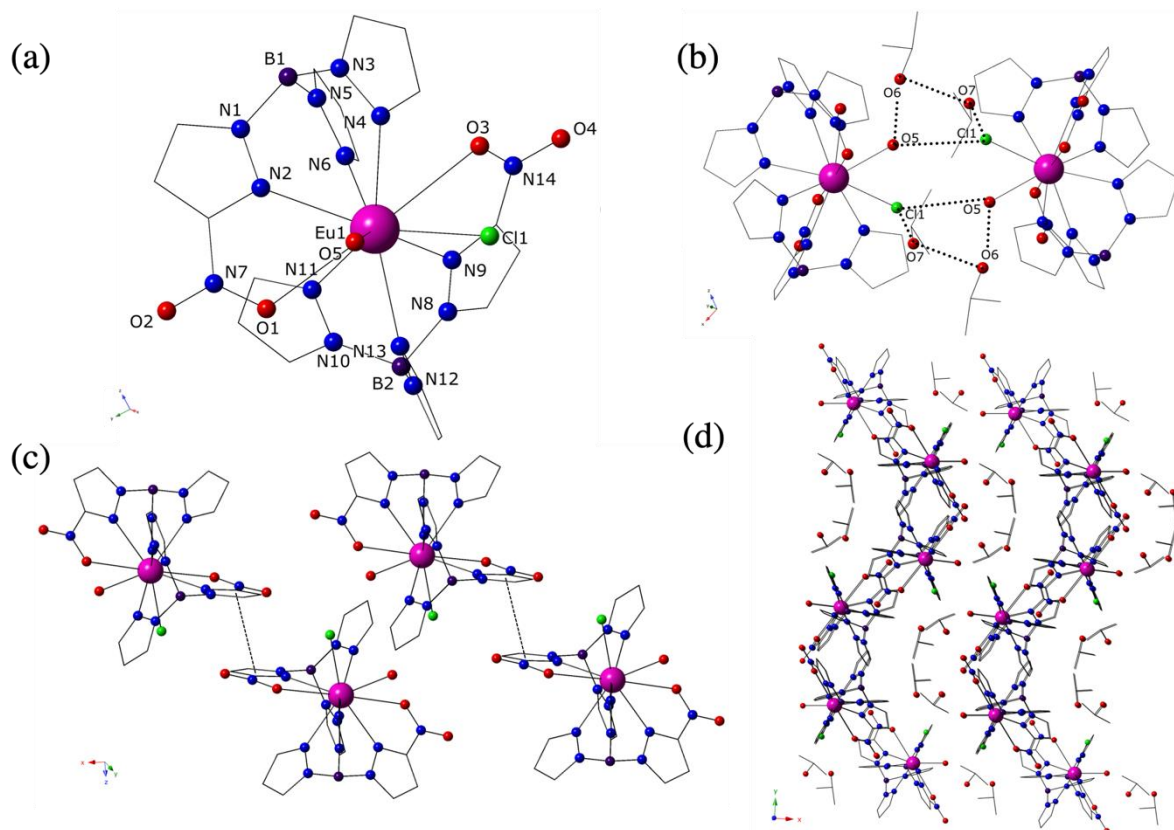


Figure 6: (a) Asymmetric unit of **3-Eu** (solvent molecules were omitted for clarity. b) Adjacent monomers of **3-Eu** form dimers with 4 unique hydrogen bonding interactions. (c) Offset π - π stacking interactions between the nitroprazole rings of adjacent dimers. (d) Packing diagram of **3-Eu** along the *c* axis.

2.2.2. Dinuclear Complexes, $[\{\text{Ln}(\text{3-NO}_2\text{Tp})_2\}_2(\mu_2\text{-CO}_3)] \cdot \text{MeOH}$ (**4-Ln**, Ln = La – Gd, except Pm)

Only six of the seven analogues of **4-Ln** (Ln = La – Eu, except Pm) yielded suitable crystals for single crystal X-ray diffraction, whereas **4-Gd** was a mostly amorphous solid (ESI Figure S7). The six analogues from La to Eu are isomorphous and only the structural details of Nd complex will be discussed. **4-Nd** crystallizes in the $C2/c$ space group with only half of the metal complex and a half-occupied methanol molecule making up the asymmetric unit. There is one unique Nd^{3+} ion coordinated to two tetradentate $\text{3-NO}_2\text{Tp}^-$ ligands with Nd1–N (N2, N4, N6, N9, N11, N13) distances ranging from 2.590(3) Å to 2.671(3) Å and Nd1–O_{NO2} (O1, O3) distances are 2.822(3) Å and 2.873(3) Å respectively. The coordination sphere is completed by a chelating *carbonate* ligand with Nd1–O (O5, O6) distances of 2.418(3) Å and

2.561(2) Å. The Nd³⁺ ion has a coordination number of ten and adopts a distorted square anti-prism geometry, analogous to that of the ten coordinate monomers in **1**-Ln (Ln = Gd, Er) and **3**-Eu. The complete, charge balanced molecule consists of two Nd³⁺ ions coordinated to four 3-NO₂Tp⁻ ligands with a bridging carbonate ligand connecting the Nd³⁺ centers (Figure 7(a)) with intramolecular Nd—Nd distances of 5.121(8) Å. These dimers assemble *via* offset π - π stacking interactions between the nitropyrazole rings of neighboring 3-NO₂Tp⁻ ligands with Cg \cdots Cg distances of 3.457(5) Å and $\beta = 9.5^\circ$ (Figure 7(b)).

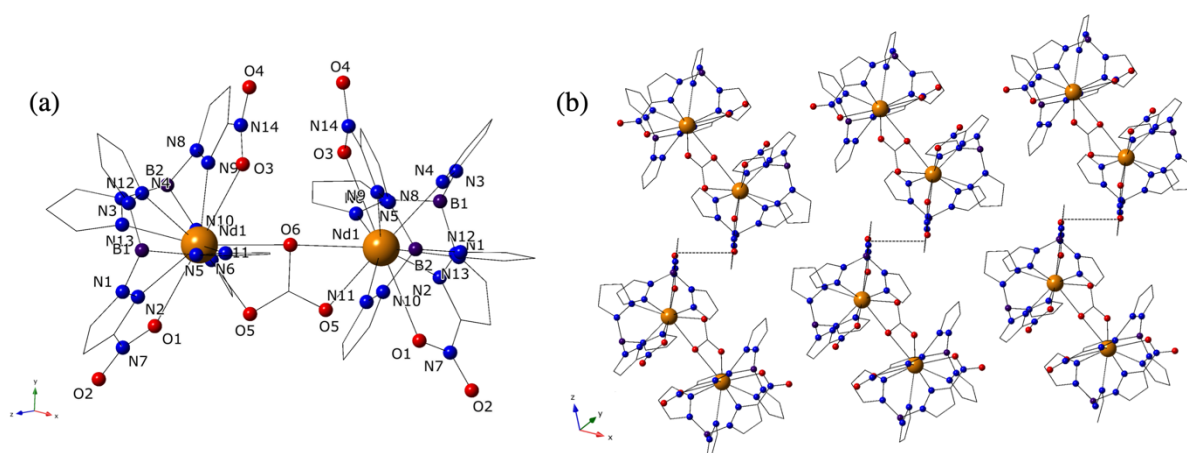


Figure 7: (a) Complete, charged balanced complex of **4**-Nd featuring a bridging *carbonate* ligand (solvent molecule was omitted for clarity). (b) Offset π - π stacking interactions between the nitropyrazole rings of adjacent dimers.

2.2.3. Tetranuclear Complexes, [$\{\text{Ln}(3\text{-NO}_2\text{Tp})\}_4(\mu_2\text{-OMe})_6(\mu_4\text{-O})$] (**5**-Ln, Ln = Pr – Tb, except Pm)

All six analogues of **5**-Ln (Ln = Pr – Tb, except Ln = Pm) are isomorphous, differing only in the identity of the Ln³⁺ center, hence only the Tb complex will be discussed in detail. **5**-Tb crystallizes in the $P2_1/n$ space group with four unique Tb³⁺ centers in a tetrahedral arrangement, where the intramolecular Tb³⁺—Tb³⁺ distances range from 3.6502(8) Å to 3.6814(7) Å and Tb-O-Tb angles from 59.76(1)° to 60.53(1)°. Each Tb³⁺ center is coordinated by one tetradentate 3-NO₂Tp⁻ ligand, three bidentate, bridging methoxide ligands and a tetradentate, bridging oxide (O²⁻) ligand at the center of the Tb₄O tetrahedron. Tb—N distances

and Tb–O (methoxide and oxide) distances range between 2.533(7) Å and 2.602(9) Å and 2.234(5) Å and 2.308(6) Å respectively, whereas Tb–O_{NO2} distances are between 3.05(1) Å and 3.18(1) Å (Figure 8(a)). The TbN₃O₅ polyhedron adopts a distorted dodecahedral coordination geometry (Figure 8(b)). Significant disorder of the nitro-groups was present in all of the structures of the various analogues of **5**-Ln, and they were modelled over three positions for each 3-NO₂Tp⁻ ligand. There are no significant non-covalent interactions between the tetramers in **5**-Tb (Figure 8).

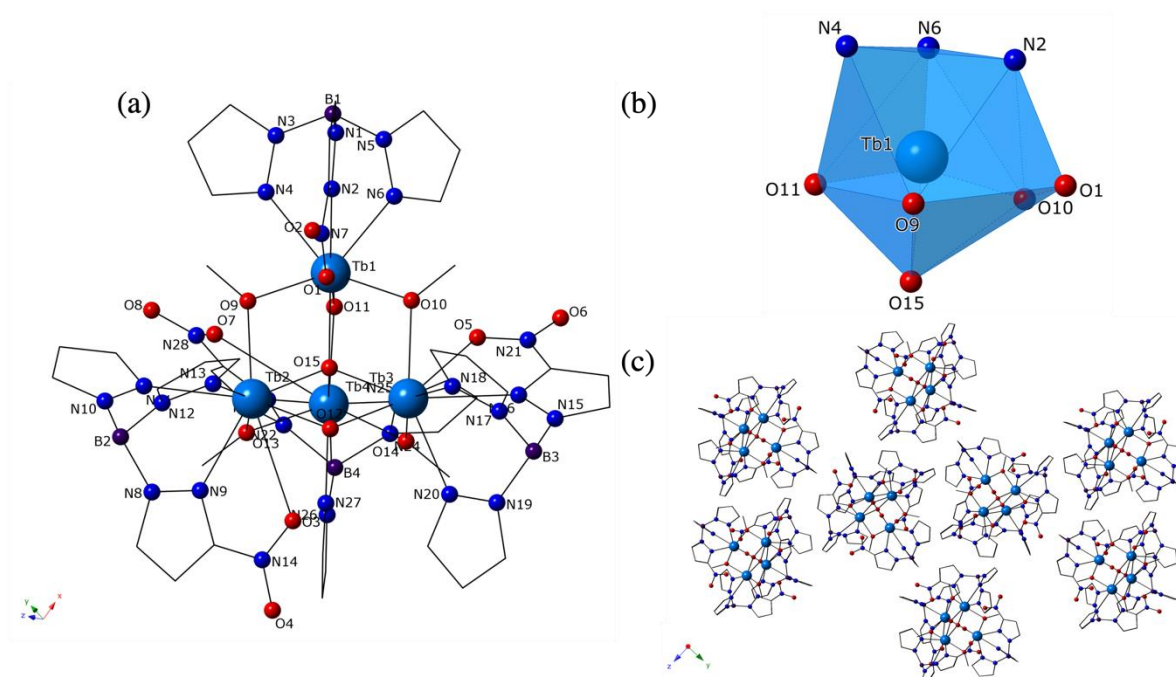


Figure 8: (a) Asymmetric unit of **5**-Tb. (b) TbN₃O₅ polyhedron displaying distorted dodecahedral geometry. (c) Packing diagram of discrete tetramers of **5**-Tb.

2.3. Criteria for the Formation of Ln(3-NO₂Tp)_x Complexes

The impressive structural diversity and tunable nuclearity of the title complexes are dependent on three major factors: lanthanide size, counterion and solvent, from most to least important. The first major criterion for the isolation of a given Ln(3-NO₂Tp)_x species is the size of the lanthanide cation. Ytterbium and lutetium can only accommodate one 3-NO₂Tp⁻ ligand, hence, they always form **2**-Ln (Figure 9). For lanthanides larger than Yb, they are split

into two groups, lanthanum to terbium, Group 1, and dysprosium to thulium, Group 2. Group 1 features lanthanide 3-nitrotrispyrazolylborates with tunable nuclearity in the form of **1-Ln** and **3-Eu** (monomers), **4-Ln** (dimers) and **5-Ln** (tetramers), whereas Group 2 only contains the isomorphous, nitrate monomers of **1-Ln** ($\text{Ln} = \text{Dy} - \text{Tm}$). Nitrate salts yield **1-Ln**, whereas chloride salts do not generate crystalline product in methanol, except for **3-Eu**, which was isolated from an isopropanol solution. Of the nitrate monomers of **1-Ln** in Group 1, most belong to the polymorph with ten coordinate monomers only (**1-La** – **1-Gd**), whereas **1-Tb** belongs to the same phase as the complexes from Group 2.

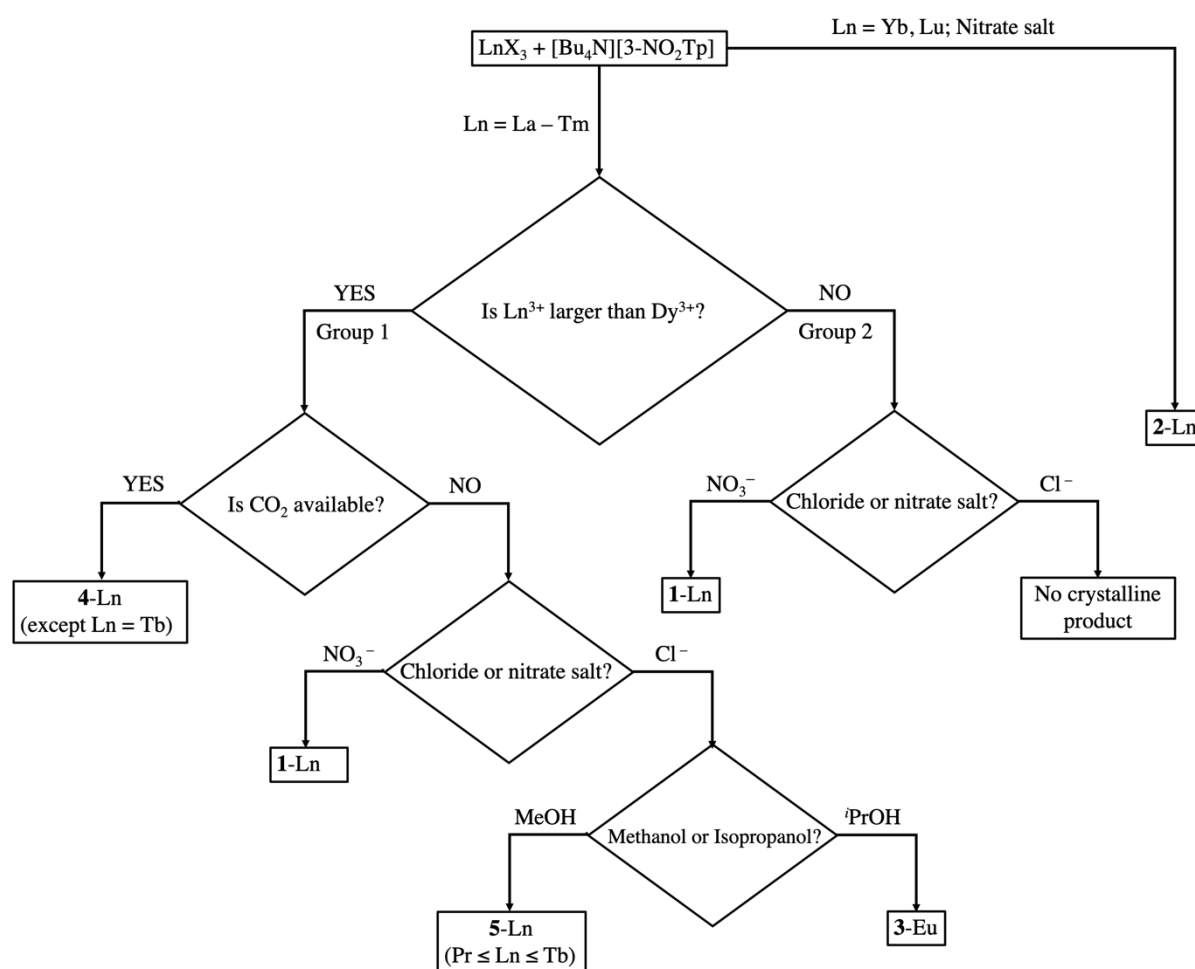


Figure 9: Schematic diagram of the product distribution of $\text{LnX}_3 + 3\text{-NO}_2\text{Tp}^-$ showing the effect of the identity of counterion, X and the solvent, as well as availability of CO_2 .

After accounting for the size of the lanthanide, the primary criterion that determines which $\text{Ln}(\text{3-NO}_2\text{Tp})_x$ complex is isolated is the presence of atmospheric CO_2 . If the reaction mixture is allowed to evaporate in open air, then **4-Ln** is isolated for $\text{Ln} = \text{La} - \text{Gd}$. **4-Tb** has never been isolated and the very low yields of **4-Gd** (5 %) suggest that gadolinium is the smallest lanthanide that can form **4-Ln**. The yields and purity of **4-Ln** can be improved by using the chloride salts (to avoid co-forming **1-Ln**) and using a 1:2 Ln^{3+} :3- NO_2Tp ratio. Once both **1-Ln** and **4-Ln** have been eliminated as possibilities, then **5-Ln** ($\text{Ln} = \text{Pr} - \text{Tb}$), or **3-Eu** if the solvent is isopropanol, can be isolated in decent to good yields (Figure 9). If **5-Ln** is the desired product, the possibility of co-forming either **1-Ln** or **4-Ln** can be minimized by using chloride salts (to eliminate **1-Ln**) while removing/reducing available CO_2 (**4-Ln**), by either slow evaporation under inert atmosphere or precipitation from the reaction mixture in a sealed vial. **5-Ln** features the well-known Ln_4O_7 tetrahedral moiety³¹ that is typically associated with the ligand-controlled hydrolysis of lanthanide ions¹⁸ and the synthesis criteria for Ln_4O_7 clusters will be discussed in a later section.

These results differ drastically from the coordination chemistry of Tp^- , where LnTp_3 is typically the product whenever LnX_3 ($\text{Ln} = \text{La} - \text{Yb}$, $\text{X} = \text{Cl}, \text{NO}_3$) reacts with Tp^- without any co-ligands.³² The introduction of a nitrated pyrazole ring to Tp^- increased the steric bulk and therefore, the hypothetical $\text{Ln}(\text{3-NO}_2\text{Tp})_3$ does not form as the nitro-group can act as an additional binding site, resulting in steric congestion around the lanthanide center when more than two 3- NO_2Tp^- ligands are coordinated. The combined effects of the steric bulk of 3- NO_2Tp^- and the lanthanide contraction result in the observed structural diversity of $\text{Ln}(\text{3-NO}_2\text{Tp})_x$ complexes.

CO₂ Capture in **4**-Ln

The bridging *carbonate* ligand present in **4**-Ln is result of atmospheric CO₂ dissolving into the methanol reaction mixture, forming carbonic acid, H₂CO₃. The formation of **4**-Ln is fully prevented by conducting the reaction under inert atmosphere, indicating that the *carbonate* ligand is generated *in situ* as the product of metal-assisted deprotonation of H₂CO₃ to CO₃²⁻. Given the low solubility of CO₂ in methanol, we surmise that the process is driven by the crystallization of **4**-Ln out of solution. The yields of **4**-Ln, up to 44 %, occur under ambient atmospheric conditions, highlight the possible application of Ln(3-NO₂Tp)_x complexes for CO₂ sequestration.

Ligand-controlled solvolysis of lanthanide ions without external base in **5**-Ln

Ligand-controlled hydrolysis/solvolysis of metal ions is a well-established synthetic strategy towards discrete polynuclear complexes *via* the deprotonation of coordinated water or solvent molecules under neutral or basic conditions.^{18, 33} In most examples of ligand-controlled lanthanide hydrolysis however, an external base, such as Et₃N or NaOH, is usually implemented as a sink for H⁺ ions and to push the reaction equilibrium towards to hydrolysis product. **5**-Ln features methoxide (μ_2 -MeO⁻) and oxo (μ_4 -O²⁻) ligands, bridging Ln³⁺ ions, in a fashion reminiscent of the products of ligand-controlled lanthanide hydrolysis, but without any external base, which is typically necessary to form the desired M_nO_m units. In a manner similar to the *in situ* formation of CO₃²⁻ in **4**-Ln, the methoxide and oxo ligands are formed *via* metal-assisted deprotonation of solvent, methanol and water molecules, respectively. Isopropanol was used to test the ability of the synthetic conditions to deprotonate alcohols other than methanol and **3**-Eu was the product, not **5**-Eu. This result revealed that the alcohol must have a pK_a less than 17.1 to facilitate ligand-controlled lanthanide solvolysis under the reaction conditions.

The solid state structures of the various $\text{Ln}(3\text{-NO}_2\text{Tp})_x$ complexes suggests there may be well-defined molecular building blocks in solution. Solution studies such as, NMR and soft ionization mass spectrometry, may provide insight into the self-assembly of the *carbonate* bridged dimers of **4**-Ln and the metal solvolysis necessary to generate the tetramers of **5**-Ln from these building units.

2.4. Infrared Spectroscopy

The analysis of the crystal structures of **n**-Ln revealed long Ln–O_{NO₂} bond lengths in most of the title complexes, suggesting that the O atoms in the nitro-group are coordinated to the lanthanide centers. We used infrared spectroscopy to further probe the coordination of the nitro-groups to metal ions. The asymmetric and symmetric stretching frequencies, $\nu_{\text{as}}(\text{NO}_2)$ and $\nu_{\text{s}}(\text{NO}_2)$ respectively, of a free nitro-group are typically one peak each, whereas upon coordination to a metal center, $\nu_{\text{as}}(\text{NO}_2)$ and $\nu_{\text{s}}(\text{NO}_2)$ are split into two peaks. This observation has been used as evidence of the coordination of a nitro-group in picrates³⁴⁻³⁷ or nitrophenolates¹⁵ to a lanthanide center. By comparing the IR spectra of the free 3-NO₂Tp⁻ ligand and the various **n**-Ln complexes we noted a split in the asymmetric and symmetric stretching frequencies, $\nu_{\text{as}}(\text{NO}_2)$ and $\nu_{\text{s}}(\text{NO}_2)$ respectively, of the 3-NO₂Tp⁻ ligand, in most of the $\text{Ln}(3\text{-NO}_2\text{Tp})_x$ complexes. **2**-Ln being the exception, as their IR spectra lacked any splitting in the $\nu_{\text{as}}(\text{NO}_2)$ and $\nu_{\text{s}}(\text{NO}_2)$ peaks, consistent with the isolation of the anionic $[\text{Ln}(3\text{-NO}_2\text{Tp})(\text{NO}_3)_3]^-$ unit with very long Ln–O distances and no coordination through the nitro-group. **1**-La is used as a representative sample to show peak splitting. $\nu_{\text{as}}(\text{NO}_2)$ and $\nu_{\text{s}}(\text{NO}_2)$ were assigned to be 1527 and 1365 cm⁻¹ respectively in the free ligand, whereas the IR spectrum of **1**-La had peaks at 1540 and 1505 cm⁻¹, assigned as $\nu_{\text{as}}(\text{NO}_2)$ and 1370 and 1358 cm⁻¹ for $\nu_{\text{s}}(\text{NO}_2)$ (Table 1). Of note is that the splitting of $\nu_{\text{as}}(\text{NO}_2)$ and $\nu_{\text{s}}(\text{NO}_2)$ are very similar across all of the analogues of **1**-Ln, **4**-Ln and **5**-Ln suggesting that the Ln–ONO interaction is

similar in strength for all of the complexes that feature coordination through the nitro-group, regardless of lanthanide size and the nuclearity of the complex.

Table 1: Select IR data (cm^{-1}) for $3\text{-NO}_2\text{Tp}^-$, **1-La** and **2-Yb** and their assignments.³⁸

Compound	$\nu_{\text{as}}(\text{NO}_2)$	$\nu_{\text{s}}(\text{NO}_2)$
$3\text{-NO}_2\text{Tp}^-$	1527	1365
1-La	1540, 1505	1370, 1358
2-Yb	1542	1369

2.5. Optical Properties of $3\text{-NO}_2\text{Tp}^-$

We characterized the optical properties of the $3\text{-NO}_2\text{Tp}^-$ ligand by studying both the precursors (pyrazole and 3-nitropyrazole), in addition to performing time-dependent density functional theory (TD-DFT) calculations on a geometry optimized model of the ten coordinate monomer of **1-La**. **1-La** is the simplest model possible to study $3\text{-NO}_2\text{Tp}^-$ upon coordination to a lanthanide center, without any f-electrons. Population analysis of **1-La** indicated that the highest occupied and lowest unoccupied molecular orbitals associated with the pyrazole (Pz) and nitro-pyrazole ($3\text{-NO}_2\text{Pz}$) rings of $3\text{-NO}_2\text{Tp}^-$ are localized to those π systems (Figure 10) consistent with the difference in opto-electronic properties of nitrated vs non-nitrated pyrazoles.³⁰ The characteristics of the relevant singlet (S_n) and triplet (T_n) states of the pyrazole and nitro-pyrazole rings are summarized in Table 2, where T_2 is assumed to be equivalent to the T_1 energy of Tp^- from GdTp_2Cl as determined by Pavlishchuk and coworkers.³⁹

Table 2: Experimental S_1 and T_1 energies associated with $3\text{-NO}_2\text{Tp}^-$ with Reinhoudt analysis.

Localized π System	State/Term	Energy/ cm^{-1}	$\Delta E_{(S_n, T_1)}/ \text{cm}^{-1}$
Pz	S_2	30710 ^a	9430
	T_2	24350 ³⁹	
3-NO ₂ Pz	S_1	30000 ^a	8720
	T_1	21280 ^b	

a – Determined using the absorption edge of their respective reflectance spectra.

b – Derived from the first inflection point of the phosphorescence emission spectrum of **1-Gd**.

There is fair agreement between the calculated absorption and experimental reflectance spectra of **1-La**. TD-DFT calculations on **1-La** specified that the most probable transition of $3\text{-NO}_2\text{Tp}^-$, $S_0 \rightarrow S_1$, is a $\pi_{\text{Pz}} \rightarrow \pi^*_{3\text{-NO}_2\text{Pz}}$ intra-ligand charge transfer (ILCT) transition, with a calculated f -oscillator value and wavelength of 0.0171 and 358 nm respectively. The $S_0 \rightarrow T_1$ transitions of **1-La** ascribed the lowest lying triplet state to be at 420 nm, an $n_{\text{NO}_2} \rightarrow \pi^*_{3\text{-NO}_2\text{Pz}}$ ILCT transition. This prediction is consistent with the 78 K phosphorescence spectrum of **1-Gd**, as shown in Figure 10, which features an absorption band centered at 450 nm (black dotted line). Consistent with the findings of Tsaryuk^{23, 24} and de Bettencourt Dias,²⁵ nitrating the pyrazole ring lowered the energy of the lowest lying triplet state (T_1) of 3-nitropyrazole (21280 cm^{-1}) relative to the non-nitrated pyrazole (24350 cm^{-1}).

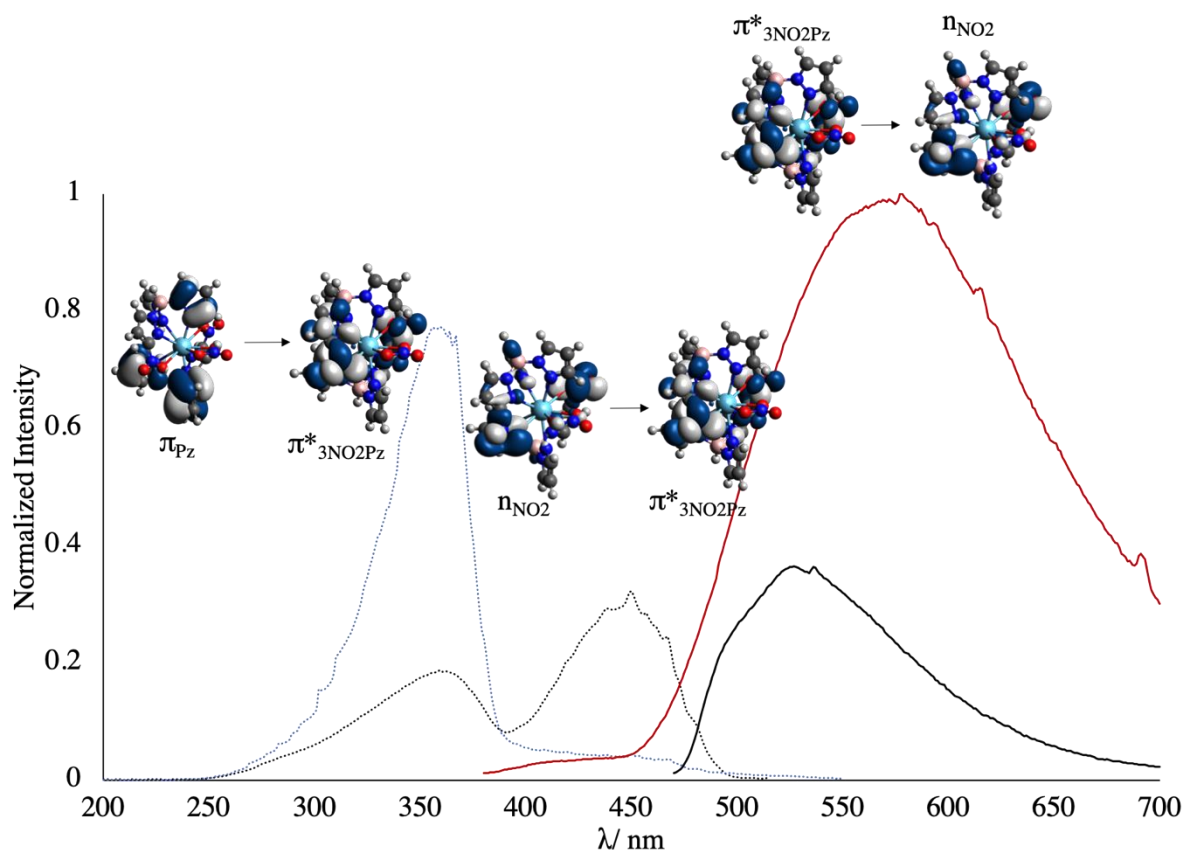


Figure 10: Photoluminescence excitation spectra (blue dotted line, obs 580 nm; black dotted line, obs 530 nm) and emission spectra (red solid line, exc 362 nm; black solid line, exc 450 nm) of **1-Gd** at 78 K with the molecular orbitals of **1-La** superimposed on top of their assigned peaks.

Using the calculated $S_0 \rightarrow S_1$ and $S_0 \rightarrow T_1$ transitions of **1-La**, all of the peaks in the phosphorescence spectra of $3\text{-NO}_2\text{Tp}^-$ (luminescence spectra of **1-Gd**) are assigned and displayed in Figure 10. The first peak at ~ 360 nm, which is present in the luminescence excitation spectra of **1-Ln** ($\text{Ln} = \text{La}, \text{Pr}, \text{Sm} - \text{Er}$), **3-Eu**, **4-Ln** and **5-Ln** ($\text{Ln} = \text{Pr}, \text{Sm}, \text{Eu}$), see Figure 10 (and ESI Figures S23 – S42), is the $\pi_{\text{Pz}} \rightarrow \pi^*_{3\text{-NO}_2\text{Pz}}$ ILCT transition. The second peak at 450 nm is an $n_{\text{NO}_2} \rightarrow \pi^*_{3\text{-NO}_2\text{Pz}}$ ILCT transition and the corresponding emission, from which the T_1 value of $3\text{-NO}_2\text{Tp}^-$ was derived, is a $\pi^*_{3\text{-NO}_2\text{Pz}} \rightarrow n_{\text{NO}_2}$ ICLT transition. These findings are consistent with the TD-DFT calculations by Raymond et al. on a model terbium nitrated-isophthalamide complex,²⁹ and the peak assignments by Tsaryuk et al. on a series of lanthanide-nitrobenzoate complexes.^{23, 24} Interestingly, all of the absorption processes

described above suggest that the 3-nitropyrazole ring dictates the photophysical properties of the 3-NO₂Tp⁻ ligand, despite the pyrazole rings outnumbering the 3-nitropyrazole rings 2 to 1.

More evidence of the 3-nitropyrazole ring dominating the properties of the 3-NO₂Tp⁻ ligand, can be seen in the excitation spectra of **1**-Ln (Ln = Pr, Sm – Er), **2**-Ln (Ln = Pr, Sm, Eu) and **5**-Ln (Ln = Pr, Sm) which feature excitation maxima from 330 – 365 nm, whereas the excitation maxima of LnTp₃ complexes are typically below 330 nm. For comparison, a fresh sample of TbTp₃ was prepared,³² and its excitation spectrum was collected and plotted, along with the analogous spectrum for **1**-Tb (Figure 11). The ligand excitation band associated with the pyrazole rings of the Tp⁻, are much narrower than the excitation band associated with the mixed pyrazole/nitropyrazole rings of 3-NO₂Tp⁻. This difference can be attributed to the contribution from the ILCT transitions in **1**-Tb that are absent in TbTp₃. In this example, it is the combination of pyrazole and nitropyrazole rings and the resultant shuttling of excited electrons across the trispyrazolylborate ligand, that broadens the band of an aromatic $\pi \rightarrow \pi^*$ transition. This represents a new mechanism to improving an antenna ligand's ability to absorb and transfer energy to the Ln³⁺ center.

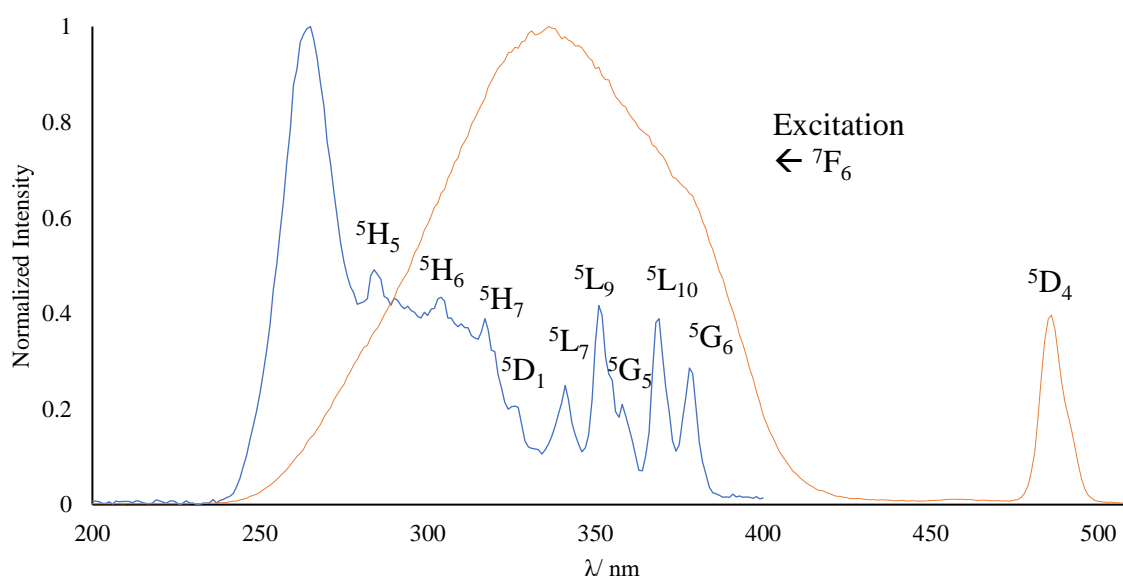


Figure 11: Room temperature excitation spectra of TbTp₃ (blue) and **1**-Tb (orange) observing the ⁵D₄ → ⁷F₅ emission at 542 nm.

2.6. Solid-state Absorption Spectroscopy

The solid-state absorption (reflectance) spectra of **n**-Ln ($n = 1 - 5$) feature a primary absorption band from 225 – 430 nm in all of the compounds, attributed to absorption by the 3-NO₂Tp⁻ ligand. **n**-Ln (Ln = Pr, Nd, Sm; $n = 1, 4, 5$), **5**-Eu, **1**-Ho, **1**-Er and **1**-Tm all feature Ln³⁺ absorptions in the visible region, in addition to the ligand absorption, whereas **1**-Sm, **n**-Eu ($n = 1, 3, 4$) display Ln³⁺ emissions in their respective reflectance spectra. Full, detailed spectra are given in the Supporting Information (Figures S11 – S24).

Interestingly, the reflectance spectra of the two Ce-containing complexes, **1**-Ce and **4**-Ce, which are yellow and bright-orange in color respectively, possess absorption edges that extend into the visible region due to an additional band from 400 – 550 nm in **1**-Ce and a much broader absorption band in **4**-Ce from 225 – 600 nm in **4**-Ce, as shown in Figure 12(a). This broad absorption into the visible region is absent in all other samples as well as the cerium starting material, Ce(NO₃)₃ and a solution of the 3-NO₂Tp⁻ ligand. We propose that a metal-to-ligand charge transfer (MLCT) transition from the 4f orbital of the Ce³⁺ ion to the π^* orbital of a 3-nitropyrazole ring of the 3-NO₂Tp⁻ ligand is likely contributing to the new absorption band. MLCT has been used to explain similar observations in some Ce³⁺ compounds that are yellow in color, given that Ce³⁺ is typically colorless/white in the solid state.⁴⁰⁻⁴² The frontier orbitals of the unoptimized monomer of **1**-Ce (using the atomic positions of the ten coordinate monomer in **1**-Gd), calculated using density functional theory (DFT), are shown in Figure 12(b). Given that the f_{xyz} orbital of Ce³⁺ are inserted as the HOMO between the pyrazole π orbitals (now HOMO-1 and HOMO-2) and the 3-nitro-pyrazole π^* orbitals (LUMO and LUMO+1) and the reducing nature of Ce³⁺, a $f \rightarrow \pi^*$ MLCT transition in **1**-Ce and **4**-Ce is probable.

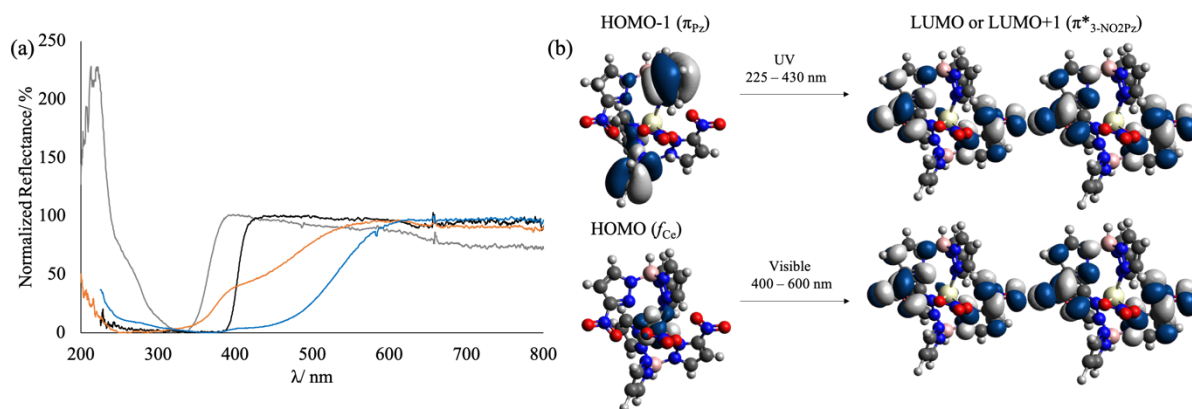


Figure 12: (a) Diffuse reflectance spectra of $\text{Ce}(\text{NO}_3)_3$ (grey), 0.02 M $[\text{Bu}_4\text{N}][3\text{-NO}_2\text{Tp}]$ (black), **1-Ce** (orange) and **4-Ce** (blue). (b) Frontier molecular orbitals of **1-Ce** calculated using DFT and suggested peak assignments for the UV and visible absorption bands, being $\pi_{\text{Pz}} \rightarrow \pi^*_{3\text{NO}_2\text{Pz}}$ and $f_{\text{Ce}} \rightarrow \pi^*_{3\text{NO}_2\text{Pz}}$ metal-to-ligand charge transfer respectively.

2.7. Photoluminescence Spectroscopy

2.7.1. Sensitized Ln^{3+} Emission

All of the reported $\text{Ln}(3\text{-NO}_2\text{Tp})_x$ complexes display sensitized Ln^{3+} emission, excluding **1-Ce** and **1-Tm**, indicating that $3\text{-NO}_2\text{Tp}^-$ is an efficient sensitizer for most of the trivalent lanthanides, even at room temperature (ESI Figures S23 – S42). Interestingly, **1-Pr**, **1-Sm**, **1-Dy**, **1-Ho** and **1-Er** all display dual visible and near-infrared emission (Figure 13), highlighting the utility of $3\text{-NO}_2\text{Tp}^-$, as an antenna ligand, capable of accessing multiple Ln^{3+} (${}^{2\text{S}+1}\text{L}_J$) states. A modified Jablonski diagram (Figure 14) was constructed to represent the various photophysical processes that lead to sensitized Ln^{3+} emission in the title **n-Ln** complexes, utilizing the information from the energy and identity of the S_n and T_n states of $3\text{-NO}_2\text{Tp}^-$.

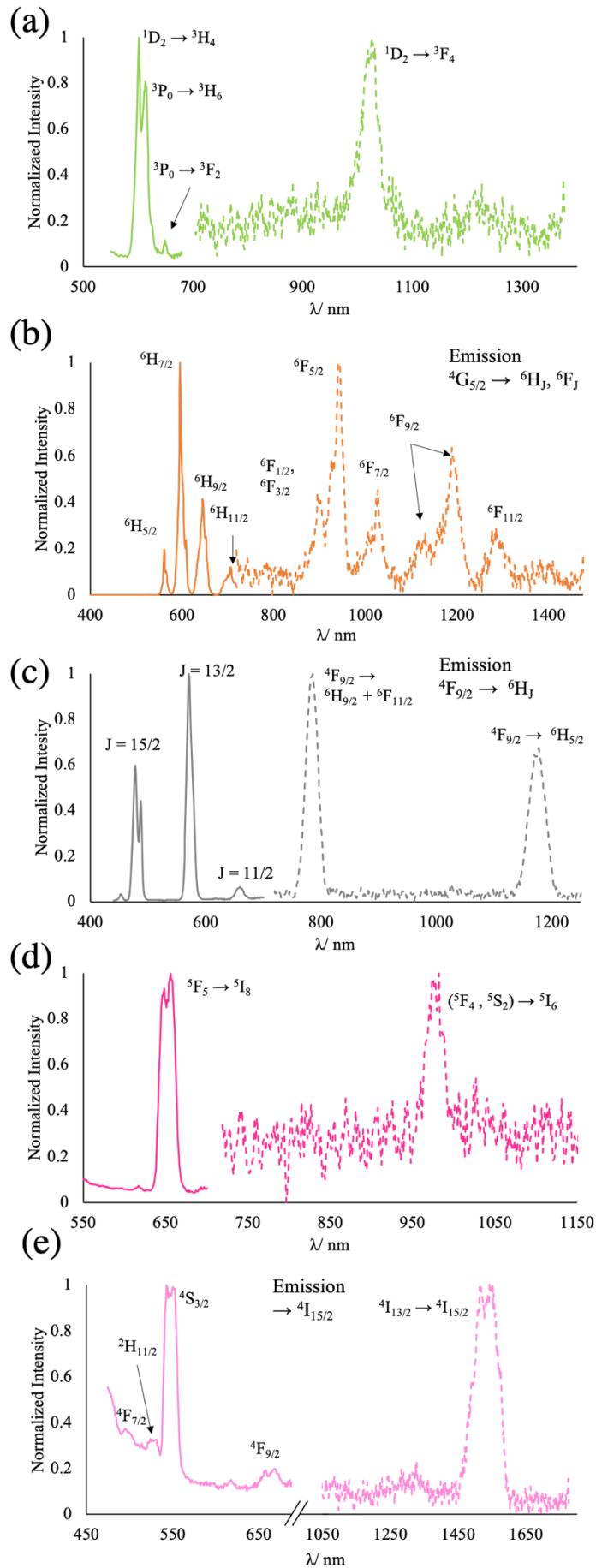


Figure 13: Dual visible (solid line) and NIR (dashed line) luminescence emission spectra of (a) 1-Pr, (b) 1-Sm, 1-Dy, 1-Ho and 1-Er with λ_{ex} ranging from 350 to 425 nm at room temperature.

1-Ce likely does not display room temperature luminescence owing to the proposed $f_{xyz}(\text{Ce}^{3+}) \rightarrow \pi^*_{3\text{-NO}_2\text{Pz}}(3\text{-NO}_2\text{Tp}^-)$ MLCT transition and subsequent non-radiative decay through π^* -n intra-ligand charge transfer (ILCT) of the 3-nitropyrazole ring. The dissipation of excitation energy via ILCT from nitrated π^* orbitals to the lone pair of O in the nitro- moiety of nitrated aromatic ligands is well documented,^{23, 24, 29} and has often been used to explain the efficient quenching of Ln^{3+} emission in lanthanide coordination compounds with nitrated ligands.^{17, 25} Interestingly, **4-Ce** does display room temperature luminescence, ascribed to metal-centered $f \rightarrow d$ transition in the UV region (ESI Figure S24). This observation could be explained by the possibility of an intervalence transition between adjacent Ce^{3+} centers in the dimers, where an electron in the f-orbital of one Ce^{3+} ion can be promoted to an empty d-orbital of the other Ce^{3+} ion in the dimer, only ~ 5 Å away. Such an intervalence transition is much less likely in the monomeric **1-Ce** with significantly longer Ce^{3+} -to- Ce^{3+} distances (~ 9 Å). While the aforementioned MLCT and non-radiative ILCT pathway may still occur in **4-Ce**, a possible intervalence transition would explain why **4-Ce** is luminescent and **1-Ce** is not.

Sensitization of lanthanide emission via the antenna effect is typically through the T_1 state of the antennae ligand.^{43, 44} As both the pyrazole and 3-nitropyrazole rings have triplet states above the emissive states of all of the **1-Ln** (except **1-Gd** and **1-Tm**), the observation of sensitized room temperature emission is therefore consistent with literature precedent. Reinhoudt and Latva have established two major criteria for good antennae ligands based on the energy difference between S_1 and T_1 states, $\Delta E_{(S_1, T_1)}$, for efficient inter-systems crossing and the energy difference between T_1 and the emissive state of Ln^{3+} , $\Delta E_{(T_1, \text{Ln})}$, respectively.⁴⁴ ⁴⁶ To summarize, Reinhoudt postulated that $\Delta E_{(S_1, T_1)} \geq 5000 \text{ cm}^{-1}$ and Latva, that $\Delta E_{(T_1, \text{Ln})} \sim 2000 - 4500 \text{ cm}^{-1}$ for most lanthanides to facilitate efficient ligand-to- Ln^{3+} energy transfer and sensitized emission. The Reinhoudt calculations have been summarized for $3\text{-NO}_2\text{Tp}^-$ in Table 2. Our ligand, $3\text{-NO}_2\text{Tp}^-$, satisfies Reinhoudt's Rule with $\Delta E_{(S_1, T_1)}$ being 8720 cm^{-1} for the S_1

and T_1 states associated with the $n_{\text{NO}_2} \rightarrow \pi^*_{3\text{-NO}_2\text{Pz}}$ ICLT transition and 3-NO₂Tp⁻-to-Ln³⁺ energy transfer. The luminescence spectra of **n**-Ln ($n = 1 - 5$; Ln = Nd, Sm, Eu, Ho, Er, Yb), which satisfy Latva's Rule, feature characteristic Ln³⁺ emissions with no observable ligand emission, i.e. efficient energy transfer from 3-NO₂Tp⁻ to the lanthanide center. The other analogues of **n**-Ln ($n = 1 - 5$; Ln = Pr, Gd, Tb, Dy, Tm) that do not satisfy Latva's Rule, will be discussed in greater detail *vide infra*.

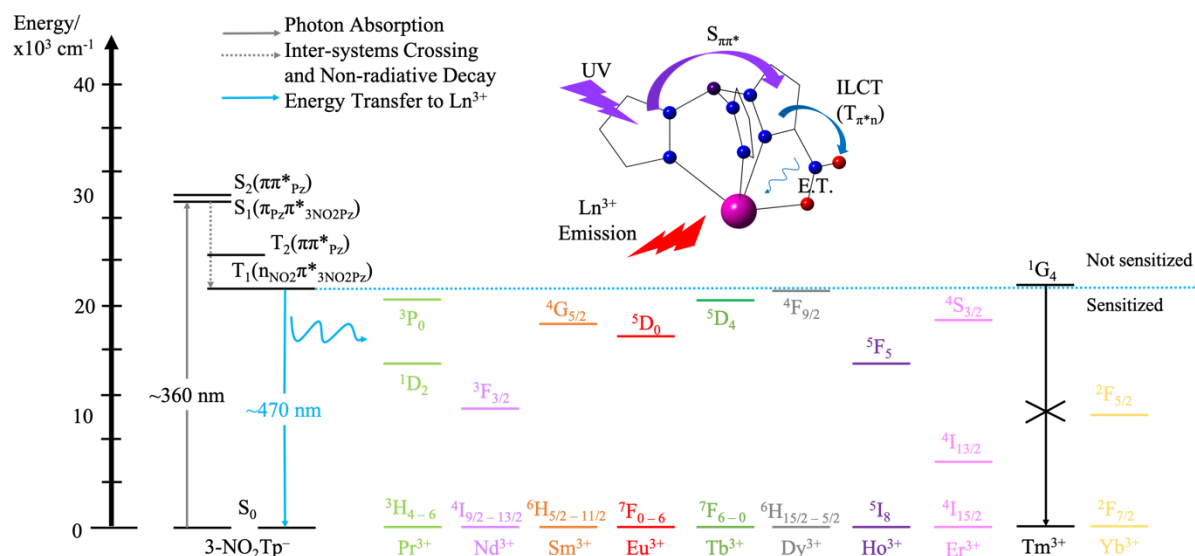


Figure 14: Modified Jablonski diagram showing energy transfer from the 3-NO₂Tp⁻ ligand to various Ln³⁺ centers, where all of the lanthanides with emissive states below the dotted, blue line display sensitized emission.

For the lanthanides that satisfy $E_{T_1}(3\text{-NO}_2\text{Pz}) \approx E(\text{Ln}^{3+}, {}^{2S+1}L_J \approx 21000 \text{ cm}^{-1})$, emission is observed, namely **n**-Pr ($n = 1, 4, 5$), **n**-Tb ($n = 1, 5$) and **1**-Dy but not **1**-Tm. For non-luminescent **1**-Tm, the resonant energy state, 1G_4 is $21,275 \text{ cm}^{-1}$,⁴⁷ is the only lanthanide state that is above the T_1 of 3-NO₂Tp⁻, with an energy difference of 5 cm^{-1} . This closeness in energy would facilitate “back-energy transfer,” between an excited Tm³⁺ (1G_4) and 3-NO₂Tp⁻ (T_1) followed by non-radiative decay *via* $\pi^*_{3\text{-NO}_2\text{Pz}} \rightarrow n_{\text{NO}_2}$ ILCT as previously described. The observation of sensitized emission from of Pr³⁺ (1P_0), Tb³⁺ (5D_4) and Dy³⁺ (${}^4F_{9/2}$) *via* $T_1(n_{\text{NO}_2} \pi^*_{3\text{-NO}_2\text{Pz}})$ with energy differences of 725 cm^{-1} , 170 cm^{-1} and 94 cm^{-1} respectively, may be attributed to the availability of higher energy, charge-separated triplet states, such as

$T_{\pi(Pz)} \rightarrow \pi^*(3-NO_2Pz)$. Such transitions are predicted by the TD-DFT calculations of both a geometry optimized $3-NO_2Tp^-$ and **1-La** and would facilitate more efficient energy transfer in **n-Ln** ($n = 1, 4$ or 5 ; $Ln = Pr, Tb, Dy$) in comparison to **1-Tm** at room temperature. Hence, **n-Ln** ($Ln = Pr, Tb, Dy$) display room temperature luminescence whereas **1-Tm** is non-luminescent.

2.7.2. Metal-Metal Interactions in Higher Nuclearity $Ln(3-NO_2Tp)_x$ Complexes

Inspection of the luminescence excitation spectra of **n-Ln** ($n = 1, 4, 5$; $Ln = Pr, Sm, Eu$) revealed a correlation between the intensity of $Ln^{3+}(^2S+1F_J)$ absorptions and the nuclearity of the $Ln(3-NO_2Tp)_x$ complexes (Figure 15). As the nuclearity of the $Ln(3-NO_2Tp)_x$ complex increases from mononuclear (**1-Ln**) to dinuclear (**4-Ln**), the Ln^{3+} absorption peaks increase in intensity, relative to the ligand absorption bands (Figure 15). This is unexpected as both **1-** and **4-Ln** have a 1:2 $Ln^{3+}:3-NO_2Tp^-$ ratio. This could be due to three possibilities: 1) lowered absorption for the $3-NO_2Tp^-$ ligand, 2) a decrease in the efficiency of $3-NO_2Tp^-$ -to- Ln^{3+} energy transfer or 3) an increase in the efficiency of Ln^{3+} -to- Ln^{3+} energy transfer (or energy migration). Possibility 1 is highly improbable given that $3-NO_2Tp^-$ coordination is unchanged across the various $Ln(3-NO_2Tp)_x$ complexes. Possibility 2 would most likely result from the coupling of the molecular vibrations of $3-NO_2Tp^-$ and the bridging *carbonate* ligands in **4-Ln**, reducing the efficiency of the $3-NO_2Tp^-$ -to- Ln^{3+} energy transfer. This hypothesis can be excluded as the relative intensity of the ligand and Ln^{3+} bands are unchanged between room temperature and 78 K (ESI Figures S26). The marked difference in the intensity of the Ln^{3+} absorptions between the monomeric **1-Ln** and dimeric **4-Ln** may therefore be attributed to the decrease in Ln^{3+} -to- Ln^{3+} distance from $\sim 9 \text{ \AA}$ to $\sim 5 \text{ \AA}$ respectively, favoring Ln^{3+} -to- Ln^{3+} energy transfer (possibility 3). While further reduction of Ln^{3+} -to- Ln^{3+} distances and increase in nuclearity in the **5-Ln** tetramers would be expected to *increase* even more the efficiency of resonant energy transfer, the Ln^{3+} /ligand absorption ratios in the excitation profiles do not

follow the expected trend for **5**-Ln, except in **5**-Eu. Possible explanations include variable Ln³⁺-to-Ln³⁺ energy transfer rates, back-energy transfer and possible concentration quenching influencing the excitation profiles of the tetramers, in addition to the effect of a 1:1 Ln³⁺:3-NO₂Tp⁻ ratio on energy transfer efficiency.

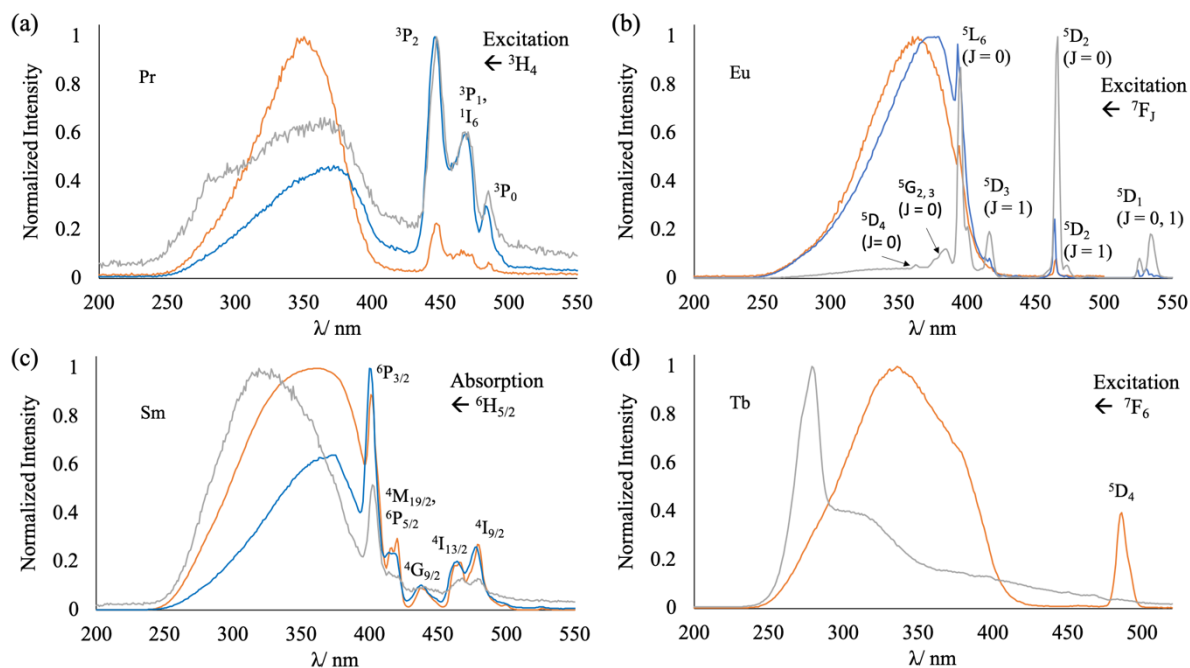


Figure 15: Room temperature excitation spectra of the Pr ($\lambda_{\text{obs}} = 611$ nm), Sm ($\lambda_{\text{obs}} = 597$ nm), Eu ($\lambda_{\text{obs}} = 614$ nm) and Tb ($\lambda_{\text{obs}} = 542$ nm) analogues of mononuclear **1**-Ln (orange), tetranuclear **5**-Ln (grey) and the Pr, Sm and Eu analogues of dinuclear **4**-Ln (blue).

The terbium analogues, **1**-Tb and **5**-Tb stand out as an exception to all of the aforementioned considerations. Given the absence of Tb³⁺ absorption present in the excitation spectra of **5**-Tb, their differing excitation spectra cannot be attributed to an increase in Ln³⁺-to-Ln³⁺ energy transfer. The hypsochromic shift observed in the ligand absorption band going from mononuclear **1**-Tb to tetranuclear **5**-Tb is ascribed to a change in the ligand molecular orbitals involved in the ligand sensitization pathway. All of the **n**-Ln complexes that featured Ln³⁺ emission has maxima in their excitation spectra at ~360 nm, a $\pi_{\text{Pz}} \rightarrow \pi^*_{3\text{-NO}_2\text{Pz}}$ ILCT transition, however the new maximum in **5**-Tb at 280 nm was consistent with a $\pi_{3\text{-NO}_2\text{Pz}} \rightarrow \pi^*_{3\text{-NO}_2\text{Pz}}$ transition based the TD-DFT calculations of **1**-La and 3-NO₂Tp⁻. Both calculations

assigned a $\pi_{3\text{-NO}_2\text{Pz}} \rightarrow \pi^*_{3\text{-NO}_2\text{Pz}}$ transition around 280 nm with f-oscillator values greater than 0.01. It is possible that energy transfer from this new $T_{\pi\pi^*(3\text{-NO}_2\text{Pz})}$ state is more efficient than the original $T_1(n\text{NO}_2 \pi^*_{3\text{-NO}_2\text{Pz}})$ state for **5**-Tb, as opposed to all of the other tetramers. The lack of any Tb^{3+} absorption peaks in **5**-Tb may be explained by concentration quenching via non-radiative decay of excited Tb^{3+} centers after energy transfer from the adjacent Tb^{3+} ions or back-energy transfer to $T_{\pi\pi^*(3\text{-NO}_2\text{Pz})}$ and non-radiative decay *via* π^* -n ILCT.

3. Conclusion

In summary, twenty-eight new lanthanide 3-nitrotrispyrazolylborate complexes have been synthesized and characterized, displaying tunable nuclearity in the form of monomers (**1**-Ln, **2**-Ln, **3**-Eu), dimers (**4**-Ln) and tetramers (**5**-Ln). In line with the unpredictable coordination geometries of the lanthanides, the coordination behavior of $\text{Ln}(3\text{-NO}_2\text{Tp})_x$ complexes is primarily driven by sterics, and by how many $3\text{-NO}_2\text{Tp}^-$ ligands can coordinate to a lanthanide center. As the size of the lanthanide ion decreases, the number of coordinated $3\text{-NO}_2\text{Tp}^-$ ligands decreases, in addition to the denticity of $3\text{-NO}_2\text{Tp}^-$, imparting structural diversity to the resultant $\text{Ln}(3\text{-NO}_2\text{Tp})_x$ complexes. Future work involving the synthesis of lanthanide complexes with different functionalized Tp^- ligands, such as $3\text{-NH}_2\text{Tp}^-$ or $4\text{-NO}_2\text{Tp}^-$, would allow us to further investigate the roles of both the nature and position of the substituent, on the structure-directing ability of this ligand platform. $3\text{-NO}_2\text{Tp}^-$ is an efficient sensitizer of most Ln^{3+} emissions (except Tm^{3+}) *via* a $\pi_{\text{Pz}} \rightarrow \pi^*_{3\text{-NO}_2\text{Pz}}$ ILCT transition, where the sensitization pathway involves excited states with charge separation between the different pyrazole rings. Moreover, a MLCT transition may be responsible for the yellow color of some Ce^{3+} -compounds, as f_{xyz} orbitals are inserted between π and π^* ligand orbitals, as the new HOMO, when an aromatic ligand is functionalized with an electron-withdrawing group. The

nitro-group being in the 3-position of the pyrazole ring and coordinated to most of the Ln^{3+} centers may have contributed to these findings, and the impact of a non-coordinated NO_2 -group (in the 4-position) would shed more light on the influence of electron-withdrawing substituents on the photophysical properties of lanthanide trispyrazolylborate complexes. Our findings of such strong electronic, $3\text{-NO}_2\text{Tp}^-$ -to- Ln^{3+} interactions (and Ln^{3+} -to- Ln^{3+} in some higher nuclearity complexes) underscore the utility of the trispyrazolylborate ligand system to design new functional materials with desirable optoelectronic properties.

Experimental Section

Materials. Lanthanide nitrate salts, $\text{Ln}(\text{NO}_3)_3 \cdot x\text{H}_2\text{O}$ ($\text{Ln} = \text{La}^{3+}, \text{Pr}^{3+}, \text{Sm}^{3+}, \text{Tb}^{3+}, \text{Dy}^{3+}, \text{Er}^{3+}, \text{Yb}^{3+}, x = 5, 6$, Strem Chemicals, 99.9%), $\text{Ln} = \text{Ce}^{3+}, \text{Nd}^{3+}, \text{Eu}^{3+}, \text{Gd}^{3+}, \text{Ho}^{3+}, \text{Tm}^{3+}, \text{Lu}^{3+}, x = 5, 6$, Aldrich, 99.9%) and lanthanide chloride salts, $\text{LnCl}_3 \cdot 7\text{H}_2\text{O}$ ($\text{Ln} = \text{La}^{3+}, \text{Ce}^{3+}$, Fisher Scientific, 99.9%), $\text{PrCl}_3 \cdot 7\text{H}_2\text{O}$ (Strem Chemicals, 99.9%), $\text{LnCl}_3 \cdot 6\text{H}_2\text{O}$ ($\text{Ln} = \text{Nd}^{3+}, \text{Sm}^{3+} - \text{Tb}^{3+}$, Aldrich, 99.9%) are commercially available and were used as received.

Synthesis of Tert-butylammonium 3-nitro-trispyrazolylborate, $[\text{Bu}_4\text{N}][3\text{-NO}_2\text{Tp}]$.

$[\text{Bu}_4\text{N}][3\text{-NO}_2\text{Tp}]$ was prepared by the procedure developed by Besson and coworkers.¹⁴ After each synthesis of $[\text{Bu}_4\text{N}][3\text{-NO}_2\text{Tp}]$, a standard solution was prepared by dissolving the reaction product in 20 mL methanol. For a given synthesis of **n-Ln**, a variable amount of the respective lanthanide salt was used to achieve the desired $\text{Ln}^{3+}:3\text{-NO}_2\text{Tp}^-$ ratio.

Mononuclear Complexes, 1-Ln. **1-Ln** can be synthesized via two routes, dependent on the solvent used methanol or isopropanol. In a typical synthesis in methanol, $\text{Ln}(\text{NO}_3)_3 \cdot x\text{H}_2\text{O}$ was dissolved in methanol (3 mL) and combined with a methanol standard solution (0.2 M) of $[\text{Bu}_4\text{N}][3\text{-NO}_2\text{Tp}]$ in a 2 dram vial in a 1:2 mole ratio for $\text{Ln} = \text{Dy} - \text{Tm}$. Single crystals of **1-Ln** were obtained for $\text{Ln} = \text{Dy} - \text{Tm}$ after slow evaporation from the open vial after 2 days. In a typical synthesis in isopropanol, $\text{Ln}(\text{NO}_3)_3 \cdot x\text{H}_2\text{O}$ was dissolved in boiling isopropanol (3 mL) and combined with a methanol standard solution (0.2 M) of $[\text{Bu}_4\text{N}][3\text{-NO}_2\text{Tp}]$ in a 2 dram vial in a 1:2 mole ratio for $\text{Ln} = \text{La} - \text{Tb}$. Crystalline powders of **1-Ln** ($\text{Ln} = \text{La} - \text{Tb}$) immediately precipitated from the isopropanol/methanol solution. Crystalline samples were isolated after 2 days *via* vacuum filtration, washed with 3x5 mL methanol and dried under vacuum for 3 – 5 minutes.

[La(3-NO₂Tp)₂(NO₃)]·0.25H₂O (**1-La**). White crystalline powder was isolated from methanol. Yield (based on La): 39 %. IR (ATR, cm⁻¹): ν = 3155 (w, -OH), 2518 (w, -BH), 1540 (m, ν_{as}-NO₂), 1548 (s, ν_{as}-NO₂), 1489 (s), 1406 (m), 1386 (m), 1370 (m, ν_s-NO₂), 1359 (m, ν_s-NO₂), 1300 (s), 1278 (vs), 1245 (w), 1217 (s), 1193 (w), 1168 (vs), 1120 (m), 1050 (vs), 1026 (m), 1018 (m), 992 (w), 973 (m), 921 (w), 889 (w), 829 (m), 816 (w), 810 (w), 789 (m), 759 (m), 752 (m), 774 (m), 731 (vs), 720 (s), 667 (m) .

[Ce(3-NO₂Tp)₂(NO₃)]·0.25H₂O (**1-Ce**). Yellow crystalline powder was isolated from methanol. Yield (based on Ce): 35 %. IR (ATR, cm⁻¹): ν = 3155 (w, -OH), 2510 (w, -BH), 1540 (s, ν_{as}-NO₂), 1506 (s, ν_{as}-NO₂), 1491 (s), 1406 (m), 1388 (m), 1370 (m, ν_s-NO₂), 1359 (m, ν_s-NO₂), 1301 (s), 1279 (s), 1245 (m), 1218 (s), 1168 (s), 1121 (m), 1108 (m), 1090 (w), 1082 (w), 1066 (m), 1050 (vs), 1026 (m), 1019 (m), 992 (w), 974 (m), 921 (w), 828 (m), 816 (w) 810 (w), 788 (m), 774 (m), 766 (m), 759 (m), 751 (m), 731 (vs), 720 (s), 668 (m).

[Pr(3-NO₂Tp)₂(NO₃)]·0.25H₂O (**1-Pr**). Green crystalline powder was isolated from methanol. Yield (based on Pr): 34 %. IR (ATR, cm⁻¹): ν = 3145 (w, -OH), 2476 (w, -BH), 1540 (m, ν_{as}-NO₂), 1505, (s, ν_{as}-NO₂), 1428 (w), 1406 (m), 1388 (m, ν_s-NO₂), 1372 (s, ν_s-NO₂), 1298 (s), 1279 (s), 1241 (m), 1218 (s), 1195 (w), 1169 (s), 1121 (s), 1109 (s), 1081 (w), 1066 (s), 1050 (vs), 1018 (m), 991 (m), 973 (s), 920 (w), 892 (w), 846 (w), 828 (s), 787 (m), 774 (m), 754 (s), 731 (vs), 720 (vs), 667 (s).

[Nd(3-NO₂Tp)₂(NO₃)]·0.25H₂O (**1-Nd**). Lilac crystalline powder was isolated from isopropanol. Yield (based on Nd): 51 %. IR (ATR, cm⁻¹): ν = 3151 (w, -OH), 2515 (w, -BH), 1541 (m, ν_{as}-NO₂), 1505, (s, ν_{as}-NO₂), 1430 (w), 1405 (m), 1387 (m), 1371 (m, ν_s-NO₂), 1359 (m, ν_s-NO₂), 1300 (s), 1279 (s), 1241 (w), 1216 (s), 1197 (w), 1187 (w), 1168 (s), 1121 (s), 1108 (m), 1081 (w), 1067 (m), 1048 (vs), 1026 (m), 1019 (m), 992 (w), 975 (s), 921 (w), 890 (w), 828 (s), 811 (w), 787 (m), 766 (s), 752 (s), 731 (vs), 719 (vs), 668 (s).

[Sm(3-NO₂Tp)₂(NO₃)]·0.25H₂O (**1-Sm**). White crystalline powder was isolated from methanol. Yield (based on Sm): 35 %. IR (ATR, cm⁻¹): $\nu = 3148$ (w, -OH), 2514 (w, -BH), 1540 (s, $\nu_{\text{as-NO}_2}$), 1494 (s, $\nu_{\text{as-NO}_2}$), 1406 (s), 1388 (s), 1373 (s, $\nu_{\text{s-NO}_2}$), 1360 (s, $\nu_{\text{s-NO}_2}$), 1311 (w), 1302 (s), 1282 (s), 1243 (m), 1218 (s), 1170 (s), 1122 (s), 1109 (s), 1067 (s), 1050 (vs), 1028 (m), 1019 (m), 974 (m), 827 (s), 812 (m), 788 (s), 773 (s), 766 (s), 751 (s), 730 (s), 720 (s), 668 (m).

[Eu(3-NO₂Tp)₂(NO₃)]·0.25H₂O (**1-Eu**). White crystalline powder was isolated from isopropanol. Yield (based on Eu): 45 %. IR (ATR, cm⁻¹): $\nu = 3150$ (w, -OH), 2500 (w, -BH), 1542 (m, $\nu_{\text{as-NO}_2}$), 1506 (s, $\nu_{\text{as-NO}_2}$), 1431 (w), 1406 (m), 1388 (m), 1373 (m, $\nu_{\text{s-NO}_2}$), 1360 (m, $\nu_{\text{s-NO}_2}$), 1312 (sh, m), 1301 (s), 1283 (s), 1242 (m), 1220 (m), 1170 (s), 1122 (m), 1109 (m), 1090 (w), 1082 (w), 1068 (m), 1050 (vs), 1027 (m), 1019 (m), 992 (w), 976 (m), 921 (w), 890 (w), 860 (w), 827 (s), 811 (m), 787 (s), 767 (s), 752 (s), 731 (vs), 720 (vs), 668 (s).

[Gd(3-NO₂Tp)₂(NO₃)]·0.25H₂O (**1-Gd**). White crystalline powder was isolated from isopropanol. Yield (based on Gd): 44 %. IR (ATR, cm⁻¹): $\nu = 3152$ (w), 2500 (w, -BH), 1544 (m, $\nu_{\text{as-NO}_2}$), 1505 (s, $\nu_{\text{as-NO}_2}$), 1478 (sh, m), 1432 (w), 1406 (m), 1388 (m), 1373 (m, $\nu_{\text{s-NO}_2}$), 1360 (m, $\nu_{\text{s-NO}_2}$), 1311 (sh, w), 1300 (s), 1282 (s), 1244 (m), 1214 (s), 1194 (w), 1169 (s), 1122 (s), 1082 (w), 1069 (s), 1049 (vs), 1027 (m), 992 (w), 976 (s), 921 (w), 889 (w), 862 (w), 828 (m), 812 (w), 787 (m), 755 (s), 723 (vs), 667 (s).

[Tb(3-NO₂Tp)₂(NO₃)] (**1-Tb**). White crystalline powder was isolated from isopropanol. Yield (based on Tb): 38 %. IR (ATR, cm⁻¹): $\nu = 3153$ (br, w), 2499 (br, w), 1544 (m, $\nu_{\text{as-NO}_2}$), 1504 (s, $\nu_{\text{as-NO}_2}$), 1484 (sh, m), 1426 (w), 1406 (m), 1389 (m), 1374 (m, $\nu_{\text{s-NO}_2}$), 1362 (m, $\nu_{\text{s-NO}_2}$), 1297 (s), 1275 (s), 1244 (m), 1218 (s), 1194 (w), 1166 (s), 1126 (m), 1085 (w), 1065 (m), 1049 (vs), 1021 (s), 990 (sh, w), 979 (m), 921 (w), 984 (w), 865 (w), 828 (m), 811 (w), 769 (s), 754 (s), 717 (vs), 669 (m).

[Dy(3-NO₂Tp)₂(NO₃)] (**1-Dy**). White, plate-like crystals were isolated from methanol. Yield (based on Dy): 48 %. IR (ATR, cm⁻¹): ν = 3156 (w), 2499 (w, -BH), 1544 (m, $\nu_{\text{as-NO}_2}$), 1505 (s, $\nu_{\text{as-NO}_2}$), 1482 (sh, m), 1428 (w), 1405 (m), 1388 (m), 1373 (m, $\nu_{\text{s-NO}_2}$), 1355 (m, $\nu_{\text{s-NO}_2}$), 1298 (s), 1275 (s), 1243 (m), 1218 (s), 1193 (w), 1165 (s), 1126 (s), 1084 (w), 1070 (s), 1049 (vs), 1020 (s), 979 (s), 920 (w), 894 (w), 826 (s), 810 (m), 796 (m), 783 (m) 769 (s), 717 (vs), 663 (s).

[Ho(3-NO₂Tp)₂(NO₃)] (**1-Ho**). Pink, plate-like crystals were isolated from methanol. Yield (based on Ho): 33 %. IR (ATR, cm⁻¹): ν = 3156 (w), 2500 (w, -BH), 1545 (m, $\nu_{\text{as-NO}_2}$), 1505 (s, $\nu_{\text{as-NO}_2}$), 1486 (sh, m), 1427 (w), 1406 (m), 1390 (m), 1375 (m, $\nu_{\text{s-NO}_2}$), 1358 (m, $\nu_{\text{s-NO}_2}$), 1298 (s), 1279 (s), 1244 (m), 1220 (s), 1193 (w), 1167 (s), 1127 (m), 1085 (w), 1070 (m), 1050 (vs), 1021 (m), 980 (s), 922 (w), 894 (w), 827 (s), 812 (m), 796 (m), 784 (s), 770 (s), 718 (vs), 669 (m).

[Er(3-NO₂Tp)₂(NO₃)] (**1-Er**). Pink, plate-like crystals were isolated from methanol. Yield (based on Er): 27 %. IR (ATR, cm⁻¹): ν = 3157 (w), 2500 (w, -BH), 1540 (m, $\nu_{\text{as-NO}_2}$), 1500 (s, $\nu_{\text{as-NO}_2}$), 1427 (w), 1405 (m), 1388 (m), 1375 (m, $\nu_{\text{s-NO}_2}$), 1357 (m, $\nu_{\text{s-NO}_2}$), 1298 (s), 1279 (s), 1245 (m), 1219 (s), 1190 (w), 1166 (s), 1136 (w), 1127 (m), 1110 (m), 1085 (w), 1071 (m), 1048 (s), 1020 (s), 981 (s), 921 (w), 895 (w), 826 (m), 811 (m), 796 (m), 784 (m), 768 (s), 753 (s), 717 (s), 663 (m).

[Tm(3-NO₂Tp)₂(NO₃)] (**1-Tm**). White, plate-like crystals were isolated from methanol. Yield (based on Tm): 21 %. IR (ATR, cm⁻¹): ν = 3367 (br, -OH), 3157 (w), 2500 (w, -BH), 1624 (w), 1541 (m, $\nu_{\text{as-NO}_2}$), 1503 (s, $\nu_{\text{as-NO}_2}$), 1428 (w), 1405 (m), 1378 (m, $\nu_{\text{s-NO}_2}$), 1358 (m, $\nu_{\text{s-NO}_2}$), 1299 (s), 1280 (s), 1246 (w), 1221 (m), 1194 (w), 1168 (m), 1128 (m), 1110 (m), 1086 (w), 1071 (m), 1050 (vs), 1022 (m), 982 (m), 923 (w), 895 (w), 827 (m), 812 (m), 797 (m), 778 (m), 770 (s), 753 (s), 731 (vs), 719 (vs) 665 (s).

Mononuclear Complexes, 2-Ln. In a typical synthesis, $\text{Ln}(\text{NO}_3)_3 \cdot x\text{H}_2\text{O}$ ($\text{Ln} = \text{Yb}, \text{Lu}$) was dissolved in methanol (3 mL) and combined with a methanol standard solution (0.2 M) of $[\text{Bu}_4\text{N}][3\text{-NO}_2\text{Tp}]$ in a 2 dram vial in a 1:2 mole ratio. Crystalline powders of **2-Ln** formed after the reaction mixture evaporated to dryness over 4 days to a 1 week. Crystalline samples were collected *via* vacuum filtration, washed with 3x5 mL isopropanol and dried under vacuum for 3 – 5 minutes. Single crystals were isolated from the bulk samples.

$[\text{Bu}_4\text{N}][\text{Yb}(3\text{-NO}_2\text{Tp})(\text{NO}_3)_3]$ (**2-Yb**). White crystals were isolated from methanol. Yield (based on Yb): 31 %. IR (ATR, cm^{-1}): $\nu = 2967$ (w), 2877 (w), 2489 (w, -BH), 2363 (w, -BH), 1542 (sh, w, $\nu_{\text{as}}\text{-NO}_2$), 1499 (s, $\nu_{\text{as}}\text{-NO}_3$), 1404 (m), 1380 (m), 1369 (m, $\nu_{\text{s}}\text{-NO}_2$), 1287 (vs, $\nu_{\text{s}}\text{-NO}_3$), 1222 (m), 1169 (m), 1125 (w), 1112 (2), 1058 (s), 1026 (s), 990 (m), 924 (w), 880 (w), 825 (m), 813 (m), 789 (m), 786 (m), 765 (s), 726 (vs), 672 (m).

$[\text{Bu}_4\text{N}][\text{Lu}(3\text{-NO}_2\text{Tp})(\text{NO}_3)_3]$ (**2-Lu**). White crystals were isolated from methanol. Yield (based on Lu): 20 %. IR (ATR, cm^{-1}): $\nu = 3170$ (w), 2971 (w), 2880 (w), 2500 (w, -BH), 1542 (sh, w, $\nu_{\text{as}}\text{-NO}_2$), 1496 (s, $\nu_{\text{as}}\text{-NO}_3$), 1405 (m), 1383 (m), 1370 (m, $\nu_{\text{s}}\text{-NO}_2$), 1286 (vs), 1225 (s), 1198 (w), 1170 (s), 1125 (m), 1114 (m), 1078 (w), 1066 (sh, m), 1059 (s), 1027 (s), 991 (m), 924 (w), 882 (w), 826 (m), 813 (m), 788 (m), 786 (m), 758 (s), 726 (s), 672 (m).

Mononuclear Complex, 3-Eu. $\text{EuCl}_3 \cdot 6\text{H}_2\text{O}$ (0.0201 g, 0.0778 mmol) was dissolved in boiling isopropanol (2.5 mL) and combined with a methanol standard solution (0.2 M) of $[\text{Bu}_4\text{N}][3\text{-NO}_2\text{Tp}]$ in a 2 dram vial in a 1:1 mole ratio. Single crystals of **3-Eu** formed after slow evaporation of the reaction mixture, in an open vial for 1 week. Crystalline samples were collected *via* vacuum filtration, washed with 3x5 mL methanol and dried under vacuum for 3 – 5 minutes.

$[\text{Eu}(3\text{-NO}_2\text{Tp})_2\text{Cl}(\text{H}_2\text{O})] \cdot 2^i\text{PrOH}$ (**3-Eu**). White crystalline powder was isolated from isopropanol. Yield (based on Eu): 9 %. IR (ATR, cm^{-1}): $\nu = 3360$ (br, -OH), 3141 (w), 2970

(w), 2482 (w, -BH), 1636 (w), 1540 (s, $\nu_{\text{as-NO}_2}$), 1502 (s, $\nu_{\text{as-NO}_2}$), 1405 (s), 1367 (s, $\nu_{\text{s-NO}_2}$), 1363 (s, $\nu_{\text{s-NO}_2}$), 1303 (s), 1230 (m), 1220 (s), 1162 (s), 1124 (s), 1108 (s), 1055 (s), 1049 (vs), 1016 (m), 977 (s), 948 (m), 826 (s), 808 (m), 785 (m), 756 (s), 732 (vs), 719 (vs), 669 (s).

Dinuclear Complexes, 4-Ln. In a typical synthesis, $\text{LnCl}_3 \cdot x\text{H}_2\text{O}$ (Ln = La – Gd, except Pm) was dissolved in methanol (3 mL) and combined with a methanol standard solution (0.2 M) of $[\text{Bu}_4\text{N}][3\text{-NO}_2\text{Tp}]$ in a 2 dram vial in a 1:2 mole ratio. Single crystals of 4-Ln (crystalline powder for Ln = Gd) formed after the reaction mixture evaporated to dryness over 3 days and were collected *via* vacuum filtration, washed with 3x5 mL methanol and dried under vacuum for 3 – 5 minutes.

$[\{\text{La}(3\text{-NO}_2\text{Tp})_2\}_2(\mu\text{-CO}_3)] \cdot \text{MeOH}$ (**4-La**). White, block crystals were isolated from methanol. Yield (based on La): 36 %. IR (ATR, cm^{-1}): $\nu = 3145$ (w, -OH), 2474 (w, -BH), 1539 (m, $\nu_{\text{as-NO}_2}$), 1500 (s, $\nu_{\text{as-NO}_2}$), 1424 (w), 1405 (m), 1389 (m, $\nu_{\text{s-NO}_2}$), 1359 (s, $\nu_{\text{s-NO}_2}$), 1296 (s), 1240 (m), 1214 (s), 1197 (w), 1170 (s), 1122 (s), 1108 (s), 1081 (w), 1065 (m), 1046 (s), 1020 (m), 991 (w), 971 (s), 925 (w), 891 (w), 846 (w), 828 (s), 805 (w), 782 (m), 762 (s), 750 (s), 730 (s), 715 (s), 666 (m).

$[\{\text{Ce}(3\text{-NO}_2\text{Tp})_2\}_2(\mu\text{-CO}_3)] \cdot \text{MeOH}$ (**4-Ce**). Orange, block crystals were isolated from methanol. Yield (based on Ce): 42 %. IR (ATR, cm^{-1}): $\nu = 3142$ (w, -OH), 2475 (w, -BH), 1539 (m, $\nu_{\text{as-NO}_2}$), 1502 (s, $\nu_{\text{as-NO}_2}$), 1411 (w), 1405 (m), 1389 (m, $\nu_{\text{s-NO}_2}$), 1360 (s, $\nu_{\text{s-NO}_2}$), 1295 (s), 1240 (s), 1213 (s), 1196 (w), 1171 (s), 1121 (s), 1108 (s), 1081 (w), 1065 (s), 1046 (vs), 1018 (s), 991 (m), 972 (s), 925 (w), 892 (m), 846 (m), 828 (s), 805 (m), 773 (m), 762 (s), 750 (s), 732 (s), 715 (vs), 666 (s).

$[\{\text{Pr}(3\text{-NO}_2\text{Tp})_2\}_2(\mu\text{-CO}_3)] \cdot \text{MeOH}$ (**4-Pr**). Green, block crystals were isolated from methanol. Yield (based on Pr): 42 %. IR (ATR, cm^{-1}): $\nu = 3143$ (w, -OH), 2474 (w, -BH), 1540 (m, $\nu_{\text{as-NO}_2}$), 1500 (s, $\nu_{\text{as-NO}_2}$), 1423 (w), 1406 (m), 1390 (m), 1374 (m, $\nu_{\text{s-NO}_2}$), 1361 (s,

ν_s -NO₂), 1295 (s), 1240 (m), 1214 (s), 1196 (w), 1171 (s), 1122 (s), 1109 (s), 1081 (w), 1065 (m), 1047 (vs), 1018 (m), 992 (w), 972 (s), 925 (w), 893 (w), 845 (w), 828 (s), 805 (w), 782 (m), 762 (s), 750 (s), 730 (vs), 715 (vs), 676 (m), 666 (m).

[{Nd(3-NO₂Tp)₂]₂(μ -CO₃)·MeOH (**4-Nd**). Light brown, block crystals were isolated from methanol. Yield (based on Nd): 21 %. IR (ATR, cm⁻¹): ν = 3145 (w, -OH), 2475 (w, -BH), 1541 (m, ν_{as} -NO₂), 1500 (s, ν_{as} -NO₂), 1429 (w), 1406 (m), 1391 (m), 1374 (s, ν_s -NO₂), 1361 (s, ν_s -NO₂), 1298 (s), 1241 (m), 1215 (s), 1196 (w), 1169 (s), 1122 (s), 1109 (s), 1081 (w), 1065 (s), 1046 (vs), 1018 (s), 991 (m), 972 (s), 925 (w), 892 (w), 846 (m), 827 (s), 807 (m), 783 (m), 762 (s), 750 (s), 731 (vs), 716 (vs), 677 (sh, m), 668 (s).

[{Sm(3-NO₂Tp)₂]₂(μ -CO₃)·MeOH (**4-Sm**). White, block crystals were isolated from methanol. Yield (based on Sm): 35 %. IR (ATR, cm⁻¹): ν = 3324 (w, -OH), 3141 (w), 2476 (w, -BH), 1540 (m, ν_{as} -NO₂), 1504 (s, ν_{as} -NO₂), 1425 (w), 1406 (m), 1383 (m), 1376 (s, ν_s -NO₂), 1362 (s, ν_s -NO₂), 1298 (s), 1241 (s), 1216 (s), 1197 (w), 1171 (s), 1123 (s), 1110 (s), 1082 (w), 1065 (s), 1047 (vs), 1019 (s), 980 (m), 974 (s), 926 (w), 895 (w), 846 (m), 827 (s), 806 (w), 783 (m), 763 (s), 730 (vs), 716 (vs), 667 (s).

[{Eu(3-NO₂Tp)₂]₂(μ -CO₃)·MeOH (**4-Eu**). White, block crystals were isolated from methanol. Yield (based on Eu): 25 %. IR (ATR, cm⁻¹): ν = 3338 (w, -OH), 3144 (w), 2476 (w, -BH), 1541 (m, ν_{as} -NO₂), 1504 (s, ν_{as} -NO₂), 1425 (w), 1405 (m), 1376 (s, ν_s -NO₂), 1362 (s, ν_s -NO₂), 1297 (s), 1241 (m), 1216 (s), 1197 (m), 1172 (s), 1123 (s), 1110 (s), 1071 (w), 1065 (s), 1047 (vs), 1019 (s), 990 (m), 974 (s), 925 (w), 896 (w), 845 (m), 827 (s), 806 (m), 783 (m), 762 (s), 732 (vs), 717 (vs), 667 (s).

[{Gd(3-NO₂Tp)₂]₂(μ -CO₃)·MeOH (**4-Gd**). White powder was isolated from methanol. Yield: 4 %. IR (ATR, cm⁻¹): ν = 3315 (w, -OH), 3141 (w), 2476 (w, -BH), 1540 (m, ν_{as} -NO₂), 1502 (s, ν_{as} -NO₂), 1414 (w), 1407 (m), 1376 (s, ν_s -NO₂), 1365 (s, ν_s -NO₂), 1299 (s), 1241 (m), 1222 (s), 1197 (w), 1168 (s), 1123 (s), 1110 (s), 1072 (w), 1056 (s), 1048 (vs), 1019

(s), 981 (m), 975 (s), 925 (w), 896 (w), 846 (w), 826 (s), 820 (w), 783 (m), 763 (s), 723 (vs), 718 (vs), 668 (s).

Tetranuclear Complexes, **5**-Ln

5-Ln can be synthesized via two routes. In a typical synthesis via route 1, $\text{LnCl}_3 \cdot x\text{H}_2\text{O}$ (Ln = Gd, Tb) was dissolved in methanol (3 mL) and combined with a methanol standard solution (0.2 M) of $[\text{Bu}_4\text{N}][3\text{-NO}_2\text{Tp}]$ in a 2 dram vial in a 1:1 mole ratio and the reaction mixture was allowed to slowly evaporate under inert atmosphere (N_2). Single crystals of **5**-Ln formed after 24 hours, however the product was isolated after the reaction mixture evaporated to dryness after 3 days. Crystalline samples of **5**-Ln were collected *via* vacuum filtration, washed with 3x5 mL methanol and dried under vacuum for 3 – 5 minutes.

In a typical synthesis via route 2, $\text{LnCl}_3 \cdot x\text{H}_2\text{O}$ (Ln = Pr, Nd, Eu, Sm) was dissolved in methanol (3 mL) and combined with a methanol standard solution (0.2 M) of $[\text{Bu}_4\text{N}][3\text{-NO}_2\text{Tp}]$ in a sealed 2 dram vial in a 1:2 mole ratio and hexanes (3 mL) were layered on top of the methanol reaction mixture. Single crystals of **5**-Ln formed after 24 hours, however the product was isolated after 2 – 4 weeks. Crystalline samples of **5**-Ln were collected *via* vacuum filtration, washed with 3x5 mL methanol and dried under vacuum for 3 – 5 minutes.

$[\{\text{Pr}(3\text{-NO}_2\text{Tp})\}_4(\mu_2\text{-OMe})_6(\mu_4\text{-O})]$ (**5**-Pr). Green, rod-shaped crystals were isolated from methanol and hexanes. Yield (based on Pr): 17 %. IR (ATR, cm^{-1}): $\nu = 2915$ (w), 2798 (w), 2456 (w), 1537 (m, $\nu_{\text{as}}\text{-NO}_2$), 1500 (s, $\nu_{\text{as}}\text{-NO}_2$), 1444 (w), 1411 (w), 1403 (s), 1381 (w), 1375 (s, $\nu_{\text{s}}\text{-NO}_2$), 1363 (s, $\nu_{\text{s}}\text{-NO}_2$), 1301 (s), 1240 (m), 1218 (s), 1196 (w), 1120 (s), 1105 (s), 1079 (w), 1064 (s), 1045 (vs), 1014 (m), 991 (w), 972 (s), 923 (w), 895 (w), 826 (s), 807 (w), 782 (m), 760 (s), 730 (vs), 719 (vs), 668 (s).

$[\{\text{Nd}(3\text{-NO}_2\text{Tp})\}_4(\mu_2\text{-OMe})_6(\mu_4\text{-O})]$ (**5**-Nd). Green, rod-shaped crystals were isolated from methanol and hexanes. Yield (based on Nd): 18 %. IR (ATR, cm^{-1}): $\nu = 3128$ (w), 2917

(w), 2801 (w), 2459 (w, -BH), 1537 (m, $\nu_{\text{as-NO}_2}$), 1499 (s, $\nu_{\text{as-NO}_2}$), 1445 (w), 1404 (m), 1376 (s, $\nu_{\text{s-NO}_2}$), 1364 (s, $\nu_{\text{s-NO}_2}$), 1302 (s), 1241 (m), 1218 (s), 1191 (w), 1163 (s), 1121 (m), 1105 (m), 1064 (s), 1044 (vs), 1014 (m), 981 (w), 973 (s), 924 (w), 895 (w), 825 (s), 752 (s), 730 (vs), 718 (vs), 669 (s).

$[\{\text{Sm}(3\text{-NO}_2\text{Tp})\}_4(\mu_2\text{-OMe})_6(\mu_4\text{-O})]$ (**5-Sm**). White, rod-shaped crystals were isolated from methanol and hexanes. Yield (based on Sm): 17 %. IR (ATR, cm^{-1}): $\nu = 3128$ (w), 2918 (w), 2803 (w), 2457 (w, -BH), 1539 (m, $\nu_{\text{as-NO}_2}$), 1499 (s, $\nu_{\text{as-NO}_2}$), 1444 (w), 1412 (w), 1405 (s), 1377 (s, $\nu_{\text{s-NO}_2}$), 1365 (s, $\nu_{\text{s-NO}_2}$), 1303 (s), 1241 (m), 1218 (s), 1192 (w), 1163 (s), 1121 (m), 1105 (m), 1072 (w), 1064 (s), 1045 (vs), 1014 (m), 980 (w), 973 (m), 924 (w), 898 (w), 825 (s), 798 (w), 753 (s), 731 (vs), 720 (vs), 670 (m).

$[\{\text{Eu}(3\text{-NO}_2\text{Tp})\}_4(\mu_2\text{-OMe})_6(\mu_4\text{-O})]$ (**5-Eu**). White, rod-shaped crystals were isolated from methanol and hexanes. Yield (based on Eu): 24 %. IR (ATR, cm^{-1}): $\nu = 3126$ (w), 2918 (w), 2805 (w), 2459 (w, -BH), 1539 (m, $\nu_{\text{as-NO}_2}$), 1499 (s, $\nu_{\text{as-NO}_2}$), 1445 (w), 1412 (w), 1404 (s), 1377 (s, $\nu_{\text{s-NO}_2}$), 1365 (m, $\nu_{\text{as-NO}_2}$), 1303 (s), 1240 (m), 1219 (s), 1192 (w), 1163 (s), 1121 (m), 1106 (m), 1056 (s), 1045 (vs), 1014 (m), 973 (m), 924 (w), 899 (w), 824 (s), 776 (m, sh), 759 (s), 731 (vs), 720 (vs), 670 (s).

$[\{\text{Gd}(3\text{-NO}_2\text{Tp})\}_4(\mu_2\text{-OMe})_6(\mu_4\text{-O})]$ (**5-Gd**). White, rod-shaped crystals were isolated from methanol. Yield (based on Gd): 6 %. IR (ATR, cm^{-1}): $\nu = 3124$ (w), 2920 (w), 2808 (w), 2459 (w, -BH), 1539 (m, $\nu_{\text{as-NO}_2}$), 1499 (s, $\nu_{\text{as-NO}_2}$), 1428 (w), 1404 (s), 1378 (s, $\nu_{\text{s-NO}_2}$), 1365 (s, $\nu_{\text{s-NO}_2}$), 1304 (s), 1240 (m), 1220 (s), 1192 (w), 1165 (s), 1121 (m), 1106 (m), 1057 (s), 1046 (vs), 1013 (m), 981 (w), 974 (m), 925 (w), 899 (w), 857 (w), 825 (s), 750 (s), 731 (vs), 721 (vs), 669 (s).

$[\{\text{Tb}(3\text{-NO}_2\text{Tp})\}_4(\mu_2\text{-OMe})_6(\mu_4\text{-O})]$ (**5-Tb**). White, rod-shaped crystals were isolated from methanol. Yield (based on Tb): 8 %. IR (ATR, cm^{-1}): $\nu = 3130$ (w), 2920 (w), 2809 (w), 2458 (w, -BH), 1540 (m, $\nu_{\text{as-NO}_2}$), 1499 (s, $\nu_{\text{as-NO}_2}$), 1445 (w), 1414 (w), 1405 (s), 1380 (s,

ν_s -NO₂), 1368 (s, ν_s -NO₂), 1304 (s), 1241 (m), 1221 (s), 1193 (w), 1165 (s), 1122 (m), 1107 (m), 1057 (s), 1045 (vs), 1014 (m), 975 (s), 925 (m), 901 (m), 859 (w), 824 (s), 753 (s), 732 (vs), 721 (vs), 668 (s).

X-ray Structure Determination. Crystals of **1-Ln** (Ln = Gd, Dy – Tm), **2-Ln** (Ln = Yb, Lu), **3-Eu**, **4-Ln** (Ln = La – Eu) and **5-Ln** (Ln = Pr – Tb, except Pm) were harvested from mother liquors and mounted on 20 μ m MiTeGen mounts. All measurements were made using monochromated microfocus Mo K α ($\lambda = 0.71073$) radiation on a Bruker D8 Quest, equipped with a Photon II detector. All reflection data were collected at 100(2) K with 0.5 ° ϕ and ω scans. The data were reduced using SAINT,⁴⁸ and empirical absorption corrections were applied using SADABS,⁴⁹ for **1-Gd**, **2-Ln** (Ln = Yb, Lu), **3-Eu**, **4-Ln** (Ln = La – Eu) and **5-Ln** (Ln = Pr – Tb, except Pm) whereas the absorption correction for **1-Dy** – **1-Tm** was applied using XABS2.⁵⁰ Structure solutions solved using intrinsic phasing were performed using the ShelXT package⁵¹ in APEX III. All data were subsequently refined using SHELXL-2014 in the program SHELXle.⁵² All atoms were refined anisotropically. Aromatic hydrogen atoms were placed in idealized positions and allowed to ride on the coordinates of the parent atom with isotropic thermal parameters (U_{iso}) fixed at 1.2 U_{eq} for all carbon atoms and at 1.5 U_{eq} for all boron atoms. Details of the X-ray diffraction experiments and crystal data are summarized in Table 3.

Table 3: Crystallographic data for **1-Ln** (Ln = Gd, Dy - Tm), **2-Ln**, **3-Eu**, **4-Ln** (Ln = La - Eu, except Pm) and **5-Ln** (Ln = Pr - Tb, except Pm).

	1-Gd	1-Dy	1-Ho	1-Er	1-Tm	2-Yb	2-Lu
CCDC no.	2100867	2100868	2100869	2100870	2100871	2100872	2100873
Formula	Gd ₄ N ₆₀ O ₂₉ B ₃ C ₇₂ H ₇₂	DyN ₁₅ O ₇ B ₃ C ₁₈ H ₁₈	HoN ₁₅ O ₇ B ₃ C ₁₈ H ₁₈	ErN ₁₅ O ₇ B ₃ C ₁₈ H ₁₈	TmN ₁₅ O ₇ B ₃ C ₁₈ H ₁₈	YbN ₁₁ O ₁₁ BC ₂₅ H ₄₅	LuN ₁₁ O ₁₁ BC ₂₅ H ₄₅
Formula weight	2957.38	740.59	743.02	745.35	747.02	859.57	861.50
Crystal System	Tetragonal	Monoclinic	Monoclinic	Monoclinic	Monoclinic	Monoclinic	Monoclinic
Space group	I4 ₁ /a	Cc	Cc	Cc	Cc	P2 ₁ /c	P2 ₁ /c
a, Å	33.921(7)	31.2963(13)	31.530(4)	31.276(11)	31.467(5)	11.648(2)	11.646(7)
b, Å	33.921(7)	9.4753(4)	9.4751(12)	9.443(4)	9.4556(11)	17.3123(19)	17.293(6)
c, Å	9.318(2)	18.6410(8)	18.7828(17)	18.648(5)	18.690(3)	17.603(4)	17.576(9)
α, °	90	90	90	90	90	90	90
β, °	90	96.212(2)	97.237(3)	96.234(8)	96.109(5)	102.229(7)	102.20(2)
γ, °	90	90	90	90	90	90	90
V, Å ³	10722(5)	5495.4(4)	5566.7(11)	5475(3)	5529.3(14)	3469(10)	3460(3)
Z	4	8	8	8	8	4	4
T, K	100(2)	100(2)	100(2)	100(2)	100(2)	100(2)	100(2)
ρ _{calc} , g cm ⁻³	1.832	1.790	1.773	1.809	1.795	1.646	1.654
μ, mm ⁻¹	2.546	2.788	2.911	3.135	3.278	2.767	2.925
λ, Mo Kα	0.71073	0.71073	0.71073	0.71073	0.71073	0.71073	0.71073
R _{int}	0.0469	0.0325	0.0541	0.0444	0.0683	0.0352	0.0703
Residuals: ^a R; R _w	0.0236; 0.0543	0.0668; 0.1662	0.0726; 0.1790	0.0458; 0.1140	0.0744; 0.1754	0.0195; 0.0416	0.0217; 0.0431
Goodness of fit	1.034	1.038	1.047	1.036	1.023	1.025	1.023
	3-Eu	4-La	4-Ce	4-Pr	4-Nd	4-Sm	4-Eu
CCDC no.	2100874	2100875	2100876	2100877	2100878	2100879	2100880
Formula	EuClN ₁₄ O ₇ B ₂ C ₂₄ H ₃₆	La ₂ N ₂₈ O ₁₂ B ₄ C ₃₈ H ₄₀	Ce ₂ N ₂₈ O ₁₂ B ₄ C ₃₈ H ₄₀	Pr ₂ N ₂₈ O ₁₂ B ₄ C ₃₈ H ₄₀	Nd ₂ N ₂₈ O ₁₂ B ₄ C ₃₈ H ₄₀	Sm ₂ N ₂₈ O ₁₂ B ₄ C ₃₈ H ₄₀	Eu ₂ N ₂₈ O ₁₂ B ₄ C ₃₈ H ₄₀
Formula weight	841.70	1402.04	1404.46	1406.04	1412.70	1424.94	1428.16
Crystal System	Monoclinic						
Space group	P2 ₁ /c	C2/c	C2/c	C2/c	C2/c	C2/c	C2/c
a, Å	12.686(3)	19.56(3)	19.572(5)	19.5408(16)	19.504(2)	19.449(5)	19.459(18)
b, Å	22.634(7)	13.363(18)	13.330(3)	13.3132(11)	13.304(1)	13.250(4)	13.257(11)
c, Å	12.753(2)	20.57(4)	20.563(5)	20.412(2)	20.553(3)	20.446(5)	20.419(15)
α, °	90	90	90	90	90	90	90
β, °	108.348(7)	96.91(5)	96.909(9)	97.052(4)	96.949(5)	97.075(5)	97.441(18)
γ, °	90	90	90	90	90	90	90
V, Å ³	3475.4(15)	5337(15)	5326(2)	5269.9(9)	5294.0(10)	5234(2)	5223(7)
Z	4	4	4	4	4	4	4
T, K	100(2)	100(2)	100(2)	100(2)	100(2)	100(2)	100(2)
ρ _{calc} , g cm ⁻³	1.609	1.746	1.753	1.775	1.774	1.808	1.817
μ, mm ⁻¹	1.944	1.666	1.775	1.915	2.027	2.310	2.468
λ, Mo Kα	0.71073	0.71073	0.71073	0.71073	0.71073	0.71073	0.71073
R _{int}	0.0473	0.0754	0.0707	0.0508	0.0342	0.0446	0.0834
Residuals: ^a R; R _w	0.0332; 0.0913	0.0468; 0.1038	0.0543; 0.1105	0.0305; 0.0767	0.0302; 0.0764	0.0392; 0.0811	0.0487; 0.0977
Goodness of fit	1.035	1.043	1.190	1.046	1.078	1.116	1.084
	5-Pr	5-Nd	5-Sm	5-Eu	5-Gd	5-Tb	
CCDC no.	2100881	2100882	2100883	2100884	2100885	2100886	
Formula	Pr ₄ N ₂₈ O ₁₂ B ₄ C ₄₂ H ₄₆	Nd ₄ N ₂₈ O ₁₂ B ₄ C ₄₂ H ₄₆	Sm ₄ N ₂₈ O ₁₂ B ₄ C ₄₂ H ₄₆	Eu ₄ N ₂₈ O ₁₂ B ₄ C ₄₂ H ₄₆	Gd ₄ N ₂₈ O ₁₂ B ₄ C ₄₂ H ₄₆	Tb ₄ N ₂₈ O ₁₂ B ₄ C ₄₂ H ₄₆	
Formula weight	1789.95	1803.27	1827.80	1834.95	1855.31	1861.99	
Crystal System	Monoclinic	Monoclinic	Monoclinic	Monoclinic	Monoclinic	Monoclinic	
Space group	P2 ₁ /n						
a, Å	11.926(2)	11.931(4)	11.8586(12)	11.835(3)	11.8263(8)	11.7918(15)	
b, Å	26.545(3)	26.514(5)	26.226(2)	26.322(11)	26.186(3)	26.134(2)	
c, Å	23.109(4)	23.089(5)	22.806(3)	22.777(13)	22.844(3)	22.774(3)	
α, °	90	90	90	90	90	90	
β, °	93.775(8)	93.948(10)	93.694(4)	93.573(14)	93.719(3)	93.840(4)	
γ, °	90	90	90	90	90	90	
V, Å ³	7300(2)	7287(5)	7078.1(13)	7082(5)	7059.7(12)	7002.3(14)	
Z	4	4	4	4	4	4	
T, K	100(2)	100(2)	100(2)	100(2)	100(2)	100(2)	
ρ _{calc} , g cm ⁻³	1.629	1.644	1.715	1.720	1.746	1.766	
μ, mm ⁻¹	2.695	2.875	3.344	3.568	3.783	4.066	
λ, Mo Kα	0.71073	0.71073	0.71073	0.71073	0.71073	0.71073	
R _{int}	0.0306	0.0704	0.0878	0.0789	0.0479	0.0776	
Residuals: ^a R; R _w	0.0347; 0.0848	0.0366; 0.0930	0.0503; 0.1036	0.0322; 0.0644	0.0364; 0.0964	0.0477; 0.1080	
Goodness of fit	1.160	1.027	1.066	1.029	1.043	1.104	

^a R = R₁ = ∑|F_o - F_c| / ∑|F_o| for observed data only. R_w = wR₂ = {∑ [w(F_o² - F_c²)²] / ∑ [w(F_o²)²]}^{1/2} for all data.

Powder X-ray Diffraction. Powder X-ray diffraction (PXRD) data on the bulk reaction products from each sample were collected on a Rigaku Miniflex (Cu Kα 2θ = 5 – 60) and analyzed using the Match! software program. The PXRD patterns of the bulk products for **1-Ln** (Ln = La – Tm, except Pm), **2-Yb**, **2-Lu**, **3-Eu**, **4-Ln** (Ln = La – Gd, except Pm) and **5-Ln** (Ln = Pr – Tb, except Pm) were used to check purity and reproducibility and are provided in

ESI Figures S1 – S8. Only pure phases of the bulk products were used in subsequent experiments.

Infrared Spectroscopy. Infrared spectra of solid samples were collected from 650 to 4000 cm^{-1} using a Bruker Tensor 27 FT-IR spectrophotometer with a diamond attenuated total reflectance (ATR) microscope objective/ATR sample holder.

^1H Nuclear Magnetic Resonance Spectroscopy. NMR spectra of 3- NO_2Pz and $[\text{Bu}_4\text{N}][3\text{-NO}_2\text{Tp}]$ were recorded on an Agilent 400 MHz spectrometer, the data were analyzed and visualized using the VNMRJ and MestReNova software packages respectively.

Photophysical Measurements. Visible and NIR solid-state luminescence measurements were taken at room temperature (and low temperature for **1-La**, **1-Gd**, **4-Pr** and **5-Eu**) of **1-Ln** (Ln = La – Er, except Ce and Pm), **2-Yb**, **4-Ln** (Ln = Ce – Eu, except Pm) and **5-Ln** (Ln = Pr – Tb, except Pm). Spectra were collected with a Horiba Jobin Yvon fluorolog-3 spectrophotometer using a 450 W xenon arc lamp combined a double excitation monochromator and double emission monochromator. For spectra in the visible region, a photomultiplier tube at 950 V was used as the emission detector, whereas for spectra in the near-IR region, a liquid nitrogen cooled, Symphony II NIR InGaAs diode array detector was used as the emission detector. Data were manipulated using the FluorEssence software package. The solid samples were mounted on a plate using non-emitting high vacuum grease for room temperature scans. Low temperature luminescence measurements were collected on solid samples under vacuum using a Janis VPF-100 cryostat equipped with UV-grade fused silica windows coupled with a Lakshore model 325 temperature controller. Samples were mounted on a quartz plate using non-emitting high vacuum grease. Diffuse reflectance spectra were collected on solid samples

at 298 K. The light source was a Mikropack DH-2000-BAL deuterium and halogen light source coupled with an Ocean Optics Flame detector. Scattered light was collected with a fiber-optic cable. Spectra were referenced with BaSO₄. Data were processed using OceanView spectroscopy software.

Computational Methods. Computational studies were conducted using the High-Performance Computing Cluster, Pegasus at The George Washington University. The frontier molecular orbitals of **1-Ce** and the calculated UV/VIS spectrum of **1-La** was calculated using Density Functional Theory (DFT) in the Gaussian 16 software (Gaussian Inc.).⁵³ The input structure for **1-Ce** and **1-La** was derived from the crystal structure of **1-Gd** using one ten coordinate monomer and substituting the relevant lanthanide center. No optimization was performed for **1-Ce** and the single point energy calculation to determine its frontier orbitals was done using both the B3LYP^{54, 55} level of theory with the modified scalar-relativistic effective core potential (ECP) basis set def2-TZVP^{56, 57} as implemented in the software with the def2-TZVP pseudopotential applied to Ce³⁺. The same approach as utilized for 3-NO₂Tp⁻ and **1-La** with the relevant ECP basis set for La,^{56, 58, 59} however, ground state optimizations were performed. Additionally, frequency calculations were performed on 3-NO₂Tp⁻ and **1-La** to determine their global minima and subsequent time-dependent DFT calculations for their expected absorption spectra. Geometry optimizations were performed on the input structure without symmetry constraints, no imaginary frequencies were present in the calculated IR and Raman spectra and 100 singlet and triplet states each were identified in the calculated absorption spectra for both 3-NO₂Tp⁻ and **1-La**.

Associated Content

Electronic Supporting Information

The Electronic Supplementary Information is available free of charge on the ACS Publications website. Crystallographic information on CCDC 2100867 – 2100886 can be obtained free of charge by contacting the Cambridge Crystallographic Data Centre, 12 Union Road, Cambridge, CB2 1EK UK, emailing data_request@ccdc.cam.ac.uk or *via* their website http://www.ccdc.cam.ac.uk/data_request/cif.

PXRD patterns, reflectance spectra and luminescence excitation and emission spectra (PDF)

Author Information

Corresponding Authors

***Claire Besson** - Department of Chemistry, The George Washington University, Washington, DC 20052, United States; orcid.org/0000-0002-0502-3610
Email: claire_besson@gwu.edu

Authors

Christopher H. Hossack - Department of Chemistry, The George Washington University, Washington, DC 20052, United States; orcid.org/0000-0002-2629-9085
Email: chossack@gwu.edu

Raymond J. Butcher – Department of Chemistry, Howard University, Washington, DC 20059, United States; orcid.org/0000-0003-2770-7076
Email: rbutcher99@yahoo.com

Christopher L. Cahill - Department of Chemistry, The George Washington University, Washington, DC 20052, United States; orcid.org/0000-0002-2015-3595

Email: cahill@gwu.edu

Author Contributions

The manuscript was written through contributions of all authors.

Notes

The authors declare no competing financial interests.

Acknowledgment

The authors would like to thank Dr. Aaron D. Nicholas, (now at Pacific Northwest National Lab) for his help with the DFT studies, and Chenyang Ma (GW) for his help with interpretation of NMR spectra. CHH acknowledges a Cosmos Scholars Neilom Foundation Meritorious Award in Technology and Society, as well as his affiliation with the Nuclear Science and Security Consortium (NSSC) lead by the University of California, Berkeley.

Bibliography

1. Zheng, X.-Y.; Kong, X.-J.; Zheng, Z.; Long, L.-S.; Zheng, L.-S., *Acc. Chem. Res.* **2018**, *51* (2), 517-525.
2. Saraci, F.; Quezada-Novoa, V.; Donnarumma, P. R.; Howarth, A. J., *Chem. Soc. Rev.* **2020**, *49* (22), 7949-7977.
3. Meihaus, K. R.; Rinehart, J. D.; Long, J. R., *Inorg. Chem.* **2011**, *50* (17), 8484-8489.
4. Meihaus, K. R.; Minasian, S. G.; Lukens, W. W.; Kozimor, S. A.; Shuh, D. K.; Tylliszczak, T.; Long, J. R., *J. Am. Chem. Soc.* **2014**, *136* (16), 6056-6068.
5. Bortoluzzi, M.; Paolucci, G.; Polizzi, S.; Bellotto, L.; Enrichi, F.; Ciorba, S.; Richards, B. S., *Inorg. Chem. Commun.* **2011**, *14* (11), 1762-1766.
6. Bortoluzzi, M.; Paolucci, G.; Gatto, M.; Roppa, S.; Enrichi, F.; Ciorba, S.; Richards, B. S., *J. Lumin.* **2012**, *132* (9), 2378-2384.
7. Cheng, J.; Ferguson, M. J.; Takats, J., *J. Am. Chem. Soc.* **2010**, *132* (1), 2-3.
8. Zhang, F.; Zhang, J.; Zhang, Y.; Hong, J.; Zhou, X., *Organometallics* **2014**, *33* (21), 6186-6192.
9. Bonath, M.; Hollfelder, C. O.; Schädle, D.; Maichle-Mössmer, C.; Sirsch, P.; Anwander, R., *Eur. J. Inorg. Chem.* **2017**, *2017* (38-39), 4683-4692.
10. Isabel, S.; Marques, N., *New J. Chem.* **1995**, *19*, 55 - 571.
11. Marques, N.; Sella, A.; Takats, J., *Chem. Rev.* **2002**, *102* (6), 2137-2160.
12. Trofimenko, S., *J. Am. Chem. Soc.* **1966**, *88*, 1842 - 1844.
13. Flötotto, H.; Secker, T.; Kögerler, P.; Besson, C., *Eur. J. Inorg. Chem.* **2019**, *2019* (43), 4621-4624.
14. Ma, C. B., Claire, Precise Control of the Degree and Regioselectivity of Functionalization in Nitro- and Amino-Functionalized Di(Trispyrazolylborato)Iron(II) Spin Crossover Complexes. ChemRxiv, 2021.
15. Bürgstein, M. R.; Roesky, P. W., *Angew. Chem., Int. Ed* **2000**, *39* (3), 549-551.
16. Bürgstein, M. R.; Gamer, M. T.; Roesky, P. W., *J. Am. Chem. Soc.* **2004**, *126* (16), 5213-5218.
17. Smith, J. A.; Singh-Wilmot, M. A.; Carter, K. P.; Cahill, C. L.; Lough, A. J.; Knee, C. S., *New J. Chem.* **2016**, *40* (9), 7338-7349.
18. Zheng, Z., *Chem. Commun.* **2001**, (24), 2521-2529.
19. Bettencourt Dias, A. d.; Viswanathan, S., *Chem. Commun.* **2004**, (8), 1024-1025.
20. Viswanathan, S.; de Bettencourt-Dias, A., *Inorg. Chem. Commun.* **2006**, *9* (5), 444-448.
21. Viswanathan, S.; de Bettencourt-Dias, A., *Inorg. Chem.* **2006**, *45* (25), 10138-10146.
22. Bettencourt-Dias, A. d.; Viswanathan, S., *Dalton Trans.* **2006**, (34), 4093-4103.
23. Tsaryuk, V.; Zhuravlev, K.; Zolin, V.; Gawryszewska, P.; Legendziewicz, J.; Kudryashova, V.; Pekareva, I., *J. Photochem. Photobiol., A* **2006**, *177* (2), 314-323.
24. Tsaryuk, V.; Kudryashova, V.; Gawryszewska, P.; Szostak, R.; Vologzhanina, A.; Zhuravlev, K.; Klemenkova, Z.; Legendziewicz, J.; Zolin, V., *J. Photochem. Photobiol., A* **2012**, *239*, 37-46.
25. de Bettencourt-Dias, A.; Bauer, S.; Viswanathan, S.; Maull, B. C.; Ako, A. M., *Dalton Trans.* **2012**, *41* (36), 11212-11218.
26. Singh-Wilmot, M. A.; Sinclair, R. A.; Kahwa, I. A.; Lough, A. J., *J. Lumin.* **2017**, *182*, 98-106.
27. Xiao Ling Huang, J. J. D., Miquel Duran, Juan Bertran, *J. Am. Chem. Soc.* **1993**, *115*, 4024 - 4030.

28. de Bettencourt-Dias, A., Introduction to Lanthanide Ion Luminescence. In *Luminescence of Lanthanide Ions in Coordination Compounds and Nanomaterials*, pp 1-48.
29. Samuel, A. P. S.; Xu, J.; Raymond, K. N., *Inorg. Chem.* **2009**, *48* (2), 687-698.
30. Dumanović, D.; Cirić, J.; Muk, A.; Nikolić, V., *Talanta* **1975**, *22* (10), 819-822.
31. Singh-Wilmot, M. A.; Kahwa, I. A.; White, A. J. P.; Williams, D. J.; Lough, A. J., *Polyhedron* **2010**, *29* (1), 270-279.
32. Apostolidis, C.; Rebizant, J.; Kanellakopoulos, B.; von Ammon, R.; Dornberger, E.; Müller, J.; Powietzka, B.; Nuber, B., *Polyhedron* **1997**, *16* (7), 1057-1068.
33. Abbati, G. L.; Cornia, A.; Fabretti, A. C.; Caneschi, A.; Gatteschi, D., *Inorg. Chem.* **1998**, *37* (15), 3759-3766.
34. Liu, S.; Liu, W.; Tan, M.; Yu, K., *J. Coord. Chem.* **1996**, *39* (2), 105-115.
35. Ayala, J. D.; Bombieri, G.; Del Pra, A.; Fantoni, A.; Vicentini, G., *Inorg. Chim. Acta* **1998**, *274* (1), 122-125.
36. Fernandes, L. C.; Matos, J. R.; Zinner, L. B.; Vicentini, G.; Zukerman-Schpector, J., *Polyhedron* **2000**, *19* (22), 2313-2318.
37. Wang, Y.-W.; Liu, W.-S.; Yu, K.-B., *Z. Anorg. Allg. Chem.* **2006**, *632* (3), 482-486.
38. Ferenc, W.; Bocian, B., *J. Therm. Anal. Calorim.* **1998**, *52* (2), 543-552.
39. Kandel, A. V.; Mikhalyova, E. A.; Zeller, M.; Addison, A. W.; Pavlishchuk, V. V., *Theor. Exp. Chem.* **2017**, *53* (3), 180-186.
40. Peacock, R. D.; Weakley, T. J. R., *J. Chem. Soc. A* **1971**, (0), 1937-1940.
41. Blasse, G.; Dirksen, G. J.; Sabbatini, N.; Perathoner, S., *Inorg. Chim. Acta* **1987**, *133* (1), 167-173.
42. Kunkely, H.; Vogler, A., *J. Photochem. Photobiol., A* **2002**, *151* (1), 45-47.
43. Weissman, S. I., *J. Chem. Phys.* **1942**, *10* (4), 214-217.
44. Latva, M.; Takalo, H.; Mikkala, V.-M.; Matachescu, C.; Rodríguez-Ubis, J. C.; Kankare, J., *J. Lumin.* **1997**, *75* (2), 149-169.
45. Steemers, F. J.; Verboom, W.; Reinhoudt, D. N.; van der Tol, E. B.; Verhoeven, J. W., *J. Am. Chem. Soc.* **1995**, *117* (37), 9408-9414.
46. van der Tol, E. B.; van Ramesdonk, H. J.; Verhoeven, J. W.; Steemers, F. J.; Kerver, E. G.; Verboom, W.; Reinhoudt, D. N., *Chem. Eur. J.* **1998**, *4* (11), 2315-2323.
47. Meshkova, S. B.; Topilova, Z. M.; Bol'shoi, D. V.; Nazarenko, N. A., *J. Appl. Spectrosc.* **2000**, *67* (5), 893-897.
48. SAINT, Version 8.34a; 2013.
49. Sheldrick, G., **2005**.
50. Parkin, S.; Moezzi, B.; A Hope, H., *J. Appl. Crystallogr.* **1995**, *28* (1), 53 - 56.
51. Sheldrick, G., *Acta Crystallogr., Sect. A* **2008**, *64* (1), 112 - 122.
52. Hubschle, C. B.; Sheldrick, George M.; Dittrich, Birger, , *J. Appl. Crystallogr.* **2011**, *44* (6), 1281 - 1284.
53. Frisch, M. J.; Trucks, G. W.; Schlegel, H. B.; Scuseria, G. E.; Robb, M. A.; Cheeseman, J. R.; Scalmani, G.; Barone, V.; Petersson, G. A.; Nakatsuji, H.; Li, X.; Caricato, M.; Marenich, A. V.; Bloino, J.; Janesko, B. G.; Gomperts, R.; Mennucci, B.; Hratchian, H. P.; Ortiz, J. V.; Izmaylov, A. F.; Sonnenberg, J. L.; Williams; Ding, F.; Lipparini, F.; Egidi, F.; Goings, J.; Peng, B.; Petrone, A.; Henderson, T.; Ranasinghe, D.; Zakrzewski, V. G.; Gao, J.; Rega, N.; Zheng, G.; Liang, W.; Hada, M.; Ehara, M.; Toyota, K.; Fukuda, R.; Hasegawa, J.; Ishida, M.; Nakajima, T.; Honda, Y.; Kitao, O.; Nakai, H.; Vreven, T.; Throssell, K.; Montgomery Jr., J. A.; Peralta, J. E.; Ogliaro, F.; Bearpark, M. J.; Heyd, J. J.; Brothers, E. N.; Kudin, K. N.; Staroverov, V. N.; Keith, T. A.; Kobayashi, R.; Normand, J.; Raghavachari, K.; Rendell, A. P.; Burant, J. C.; Iyengar, S. S.; Tomasi, J.; Cossi, M.; Millam, J. M.; Klene, M.; Adamo, C.; Cammi, R.; Ochterski, J. W.; Martin, R.

L.; Morokuma, K.; Farkas, O.; Foresman, J. B.; Fox, D. J. *Gaussian 16 Rev. A.03*, Wallingford, CT, 2016.

54. Lee, C., Yang, Weitao, Parr, Robert G., *Phys. Rev. B* **1988**, 37 (2), 785 - 789.
55. Becke, A. D., *J. Chem. Phys.* **1993**, 98 (7), 5648-5652.
56. Dolg, M.; Stoll, H.; Savin, A.; Preuss, H., *Theoret. Chim. Acta* **1989**, 75 (3), 173-194.
57. Gulde, R.; Pollak, P.; Weigend, F., *J. Chem. Theory Comput.* **2012**, 8 (11), 4062-4068.
58. Dolg, M.; Stoll, H.; Preuss, H., *Theoret. Chim. Acta* **1993**, 85 (6), 441-450.
59. Weigend, F.; Ahlrichs, R., *Phys. Chem. Chem. Phys.* **2005**, 7 (18), 3297-3305.